

VaDAR: Varstrometry for Dual AGN using Radio interferometry

EMMA SCHWARTZMAN,^{1,2} TRACY E. CLARKE,¹ KRISTINA NYLAND,¹ NATHAN J. SECRET,³ RYAN W. PFEIFLE,^{4,*}
HENRIQUE SCHMITT,¹ SHOBITA SATYAPAL,² AND BARRY ROTHBERG^{3,2}

¹*U.S. Naval Research Laboratory, 4555 Overlook Ave SW, Washington, DC 20375, USA*

²*Department of Physics and Astronomy, George Mason University, 4400 University Drive, MSN 3F3, Fairfax, VA 22030, USA*

³*U.S. Naval Observatory, 3450 Massachusetts Avenue NW, Washington, DC 20392, USA*

⁴*X-ray Astrophysics Laboratory, NASA Goddard Space Flight Center, Code 662, Greenbelt, MD 20771, USA*

ABSTRACT

Binary and dual active galactic nuclei (AGN) are an important observational tool for studying the formation and dynamical evolution of galaxies and supermassive black holes (SMBHs). An entirely new method for identifying possible AGN pairs makes use of the exquisite positional accuracy of Gaia to detect astrometrically-variable quasars, in tandem with the high spatial resolution of the Karl G. Jansky Very Large Array (VLA). We present a new pilot study of radio observations of 18 quasars ($0.8 \leq z \leq 2.9$), selected from the SDSS DR16Q and matched with the Gaia DR3. All 18 targets are identified by their excess astrometric noise in Gaia. We targeted these 18 quasars with the VLA at 2-4 GHz (S-band) and 8-12 GHz (X-band), providing resolutions of $0.65''$ and $0.2''$, respectively, in order to constrain the origin of this variability. We combine these data with ancillary radio survey data and perform radio spectral modeling. The new observations are used to constrain the driver of the excess astrometric noise. We find that $\sim 39\%$ of the target sample is likely to be either candidate dual AGN or gravitationally lensed quasars. Ultimately, we use this new strategy to help identify and understand this sample of astrometrically-variable quasars, demonstrate the potential of this method for systematically identifying kpc-scale dual quasars.

Keywords: Radio active galactic nuclei (2134) — Radio astronomy (1338)

1. INTRODUCTION

In the canonical model of galaxy evolution, the formation of more massive galaxies proceeds via a series of major and minor mergers of their smaller counterparts, in addition to gas and dark matter accretion (e.g., Schweizer 1982, 1996; Toomre & Toomre 1972; Barnes & Hernquist 1992; Hibbard & van Gorkom 1996; Somerville & Davé 2015). Most massive galaxies contain a central supermassive black hole (SMBH; Kormendy & Richstone (1995)), generally of mass $10^6 - 10^{10} M_{\odot}$. Thus, galaxy mergers should result in pairs of gravitationally-bound, synchronously feeding SMBHs that travel to the center of their host merger via dynamical friction, evolving from dual systems to binary systems that are expected to coalesce (Kormendy & Richstone 1995; Barnes & Hernquist 1992; Hopkins et al. 2008; Volonteri et al. 2016). Given the apparent scaling relations between the SMBHs and their host galaxy bulge properties, a potential co-evolution exists between an SMBH and its host galaxy (Ferrarese & Merritt 2000; Gebhardt et al. 2000; Heckman & Best 2014).

The timescale of a galaxy merger is on the order of hundreds of millions to a few billion years (Tremmel et al. 2018; Callegari et al. 2009). Dual SMBHs are precursor systems, defined as having two SMBHs with a separation beyond their mutual gravitational spheres of influence; i.e. separations of ≤ 100 kpc (Ellison et al. 2011; Liu et al. 2011; Burke-Spolaor et al. 2018). Binary systems are a more advanced stage of evolution, having separations within their mutual spheres of influence; i.e. separations ≤ 100 pc (Ellison et al. 2011; Liu et al. 2011; Rodriguez et al. 2006).

Characterization of these systems at all stages of evolution is critical for understanding SMBH evolution and co-evolution with host galaxies. This is made difficult by the lack of robust detections of dual and binary SMBH systems, particularly in the binary SMBH regime. During the course of the merger, gravitational torques drive gas towards the nuclei (e.g. Barnes & Hernquist 1992, 1996; Mihos & Hernquist 1996; Burke-Spolaor et al. 2018; Khan et al. 2020), which infalls and causes gas accretion onto the SMBHs. The SMBHs then ignite as active galactic nuclei (AGN; Hopkins et al. 2008; Hopkins & Quataert 2010; Blecha et al. 2018).

AGN pair identification methods include multiple velocity peaks and/or coronal lines in optical/infrared

* NASA Postdoctoral Program Fellow

spectroscopy (Comerford et al. 2009, 2013, 2015; Wang et al. 2009, 2017; Liu et al. 2010b, 2011, 2013; Lyu & Liu 2016; Smith et al. 2010; Xu & Komossa 2009; Barrows et al. 2013; U et al. 2013), spatially-resolved imaging in the X-ray, optical, infrared, or radio regimes (Liu et al. 2010b, 2013; Barrows et al. 2013; Liu et al. 2018, 2010a; Komossa et al. 2003; Koss et al. 2011, 2012; Bianchi et al. 2008; Piconcelli et al. 2010), and mid-infrared colors (Pfeifle et al. 2019a,b; Satyapal et al. 2017; Ellison et al. 2011, 2019). For dual AGNs, systematic searches have met with varying degrees of success. There are on the order of 50 robustly confirmed systems, many of which were originally identified serendipitously. The population is biased towards local ($z < 0.1$) redshifts and physical separation $1 < r_p < 100$ kiloparsecs, (where r_p is the physical separation, as will be demonstrated in the forthcoming literature-complete catalog of multi-AGN systems; Pfeifle 2023).

Of particular interest are candidates and confirmed systems with redshifts at which both the number density of luminous quasars and the global star formation rate density peak, often referred to as “cosmic noon,” ($1 \leq z \leq 3$, Richards et al. 2006; Madau & Dickinson 2014). However, the dynamical evolution timescales of dual and binary AGN systems are comparatively short with respect to other evolutionary stages (Tremmel et al. 2018), and thus there are a substantially lower numbers of these systems predicted on the scale of tens of kpc, as they quickly (< 1 Gyr) advance to the next stage of evolution (Tremmel et al. 2018; Merritt 2013; Chen et al. 2020; Yu 2002). This issue is further compounded by the sample pre-selection criteria and the limited resolutions and sensitivities of current telescopes, leaving an observational gap between $r_p < 6$ kpc at $z > 1$ (see Figure 1 in Chen et al. 2022a). At small separations (i.e. sub-arcsecond), the resolutions of radio interferometry, space-based optical imaging, or ground-based imaging with large apertures, adaptive optics, or optical/infrared interferometry are required.

The focus of this paper is to describe a method for using radio interferometric observations to select dual AGN candidates. The National Science Foundation’s Karl G. Jansky Very Large Array (VLA) can reach the high angular resolution necessary to detect dual and binary AGN systems with separations on sub-arcsecond scales. Given their rarity, a pre-selection strategy to select promising targets for radio follow-up is crucial.

The paper is organized as follows. In Section 2, we introduce the Varstrometry method. In Section 3, we define our target selection process. In Section 4, we describe the observations, data reduction, and analysis. We present our sample properties in Section 5 and radio spectral modeling in Section 6. Our findings are discussed in Section 7. Throughout this paper, all physical separations are the projected separation (r_p). A flat Λ CDM cosmology is adopted, with a $\Omega_\Lambda = 0.69$, $\Omega_m =$

0.31, and $H_0 = 67.7$ km s $^{-1}$ Mpc $^{-1}$ (Planck Collaboration et al. 2020).

2. VARSTROMETRY

An novel astrometric technique, previously used to detect unresolved stellar binaries (e.g., Makarov & Goldin 2016) through photometric variability-induced photocenter pseudo-motion, was applied to search for unresolved dual AGNs by Hwang et al. (2020). This technique, dubbed “varstrometry” in the context of dual AGN searches by Hwang et al. (2020), leverages the unprecedented astrometric precision of *Gaia* (Gaia Collaboration et al. 2016), which has mapped the positions, parallaxes, and proper motions of billions of stars in the Milky Way. It is sensitive enough to provide unprecedented sensitivity to the positions of hundreds of thousands of distant quasars (Brown et al. 2021). While this sensitivity has confirmed the presence of wavelength-dependent positional offsets in jetted AGNs (e.g. Makarov et al. 2017, 2019), it has also revealed the presence of astrometrically variable AGN (e.g. Shen 2021; Chen et al. 2022a). Because *Gaia* is progressively source-confused for separations less than $\sim 2''$ ($2''$ corresponds to > 12.3 kiloparsecs for $z > 0.5$; Fabricius et al. 2021), it is not capable of discerning a close secondary AGN or other extended phenomena associated with the immediate AGN environment, such as jet production. However, the sub-milliarcsecond astrometric precision of *Gaia* allows for the motions of unresolved quasars to be detected. This makes astrometric variability a new discovery space for multi-AGNs and quasars.

The orbital periods of binary and dual AGNs are respectively hundreds to millions of years (e.g., Figure 2 in Dorland et al. 2020), and thus their positions are essentially fixed on the sky. This precludes a direct motion measurement by an astrometric mission. However, AGN exhibit intrinsic, stochastic variability measurable on timescales as short as hours (Sesar et al. 2011; MacLeod et al. 2012). In a dual AGN with a separation less than the effective angular resolution of *Gaia*, two components with varying brightnesses will appear to *Gaia* to have a shifting centroid (Hwang et al. 2020).

Gaia’s resolution limits are such that, for an AGN pair system, individual light curves cannot be observed. Instead, a joint variability light curve encodes the stochastic variability of the system (see Figure 1). In cases where the apparent photocenter of the AGN is different from that of its host galaxy (e.g., a disturbed/merger system or a system in which the AGN obscuration level changes rapidly), the joint variability lightcurve of that system will be indistinguishable from that of a dual AGN system. Additionally, the varstrometry technique is not only sensitive to AGN pair systems but can also select samples contaminated with star+quasar superposition systems (Pfeifle et al. 2023), lensed quasar systems (e.g. Mannucci et al. 2022; Ciurlo et al. 2023; Inada et al. 2012, 2014; O’Dowd et al. 2015), and any other morphol-

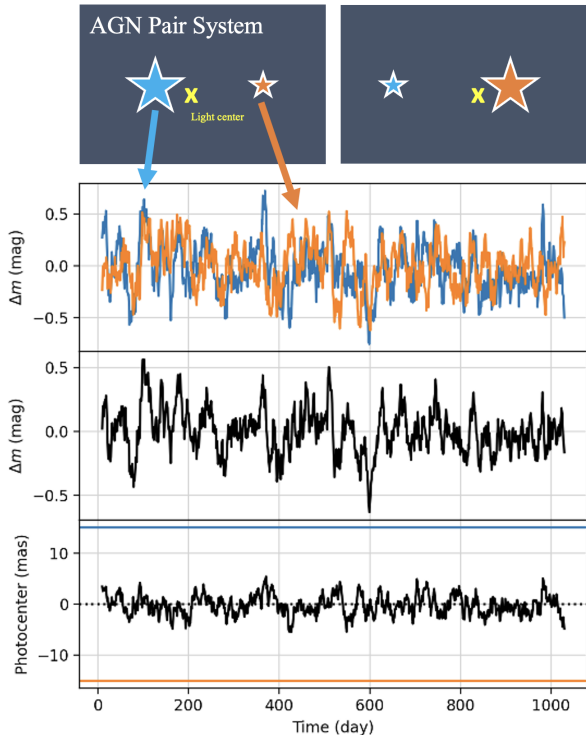


Figure 1. The Varstrometry Technique: Top: A cartoon illustrating the stochastic variability of a dual AGN including the shifting of the light center between the two component AGN. Bottom: As an example, an AGN photometric lightcurve simulation, as seen by *Gaia*, described by a first-order continuous autoregressive process (e.g. damped random walk; MacLeod et al. 2010) with $\tau = 10$ dy. A typical variability amplitude for AGN of about 0.1 magnitudes was assumed (e.g. Sesar et al. 2011), as well as a pair angular separation of 30 milliarcseconds. The middle plot shows a joint variability lightcurve, which in itself indistinguishable from systems where the apparent photocenter of the AGN is different from that of its host galaxy. The bottom plot shows the astrometric “jitter:” the photocenter of the pair appears to wander back and forth. Top figures adapted from Shen (2021).

ogy that might also drive the excess astrometric noise seen in AGN pair systems (e.g. single AGN in a host galaxy with bright stellar features).

In the case of AGN pair systems, as the mutual photocenter of the AGN pair wanders between the individual AGNs (again depending on their variability), *Gaia* measures a positional “jitter,” which is representative of the astrometric variations. This measurement also provides a lower limit on the possible physical separation for the AGN pair (σ_{astro} ; Hwang et al. 2020). For a pair of quasars with similar mean fluxes and rms fluctuations, the expected variability amplitude σ_{astro} is

$$\sigma_{astro} \approx \frac{D}{2} \frac{\sqrt{\langle \Delta f^2 \rangle}}{\bar{f}}, \quad (1)$$

where D is the separation of the component sources, and \bar{f} and $\sqrt{\langle \Delta f^2 \rangle}$ are the total mean and rms fluxes of the unresolved system. Assuming a typical fractional rms of $\sim 10\%$ (e.g. MacLeod et al. 2012), one can calculate the expected astrometric “jitter” to be ~ 10 milliarcseconds for every $0.2''$ of angular separation. Note that this measurement is a lower limit on the angular separation.

High spatial resolution follow-up has been successful for varstrometry-selected samples. Chen et al. (2022a) followed-up a sample of 84 *Gaia*-identified AGN pair candidates with the Hubble Space Telescope (HST) and Gemini GMOS optical spectroscopy. Their search revealed two previously unknown dual AGN candidates (Chen et al. 2022a; Shen 2021; Chen et al. 2022b). They conclude that $\sim 40\%$ of their HST resolved pairs are likely to be physical quasar pairs or gravitationally-lensed quasars (Chen et al. 2022a).

In this work, we present the first results from a pilot VLA program of varstrometry-selected sources (Hwang et al. 2020). Each source has excessive astrometric variability as measured by *Gaia*. Our primary goal is to place constraints on the morphology of the targets and fully characterize the sample using high-resolution radio interferometric follow-up observations. In particular, we aim to identify any potential AGN pair candidate systems, to robustly constrain the morphologies, luminosities, and radio spectra of the sample in order to understand the sample that the radio+varstrometry method selects for, constrain the driver of the excess astrometric variability, and to gauge the efficiency of the radio+varstrometry method as a pre-selection for more systematic searches for AGN pairs.

3. TARGET SELECTION

The pilot sample of quasars for this study was selected from the SDSS quasar catalog for DR16 (DR16Q; Lyke et al. 2020), which contains the most complete sample of bona fide spectroscopically-confirmed quasars from SDSS/BOSS. DR16Q was cross-matched to *Gaia*’s Early Data Release 3 (EDR3; Gaia Collaboration et al. 2016) to within $1.5''$, ensuring spectroscopic fiber coverage of the *Gaia* counterpart (Fabricius et al. 2021).

There are several *Gaia* parameters that can act as indicators of positional noise in a target, as well as more that can be manipulated to search for AGN pair systems. For this sample, the important *Gaia* parameter (see Table 1) is `astrometric_excess_noise` (AEN; the previously mentioned astrometric “jitter”), and it is defined as the amount of statistical dispersion required such that *Gaia*’s astrometric solution for the source leaves no unexplained variance (Lindgren et al.

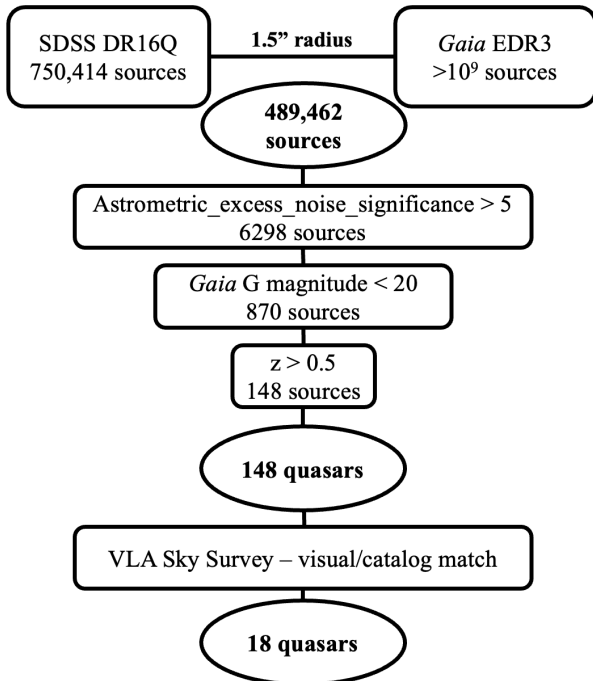


Figure 2. Target Selection: A flowchart summarizing the process of sample selection.

2021). *Gaia* also calculates the statistical significance of this value: `astrometric_excess_noise_significance` (AENS). Limiting to sources with AENS > 5 ensured a highly statistically significant measurement of excess astrometric noise in the *Gaia* astrometric solution for each target.

As *Gaia*’s astrometry is inherently optimized for compact/unresolved sources (Makarov et al. 2012; Makarov & Secrest 2022), quasars with large, extended host galaxies will exhibit spurious astrometric excess noise, as *Gaia*’s scanning window (~ 18 pixels along-scan by ~ 12 pixels across scan for the main astrometric field chips; *Gaia* Collaboration et al. (2016)) is filled by the host galaxy (Makarov & Secrest 2022; Souchay et al. 2022). This can be mitigated by making a cut on redshift, which we do here, of $z > 0.5$ (where $1''$ is ~ 6.1 kiloparsecs). We also make a cut on the *Gaia* G magnitude of $G < 20$, as there is an over-abundance of sources near *Gaia*’s sensitivity limit with high AEN, likely due to the current limitations of *Gaia*’s astrometric pipeline (Hwang et al. 2020). After applying these limits on the sample, 148 systems remain.

It is generally accepted that between 1-10% of AGN are typically radio bright (Osterbrock 1993, 1989), so it was necessary to cross-match the 148 quasars remaining to various radio surveys before committing to pointed radio observations. The larger sample was matched to the VLA Sky Survey (VLASS; Lacy et al. 2019) in order to confirm the existence of a radio signature. The

final sample was composed of 18 targets (see Table 2) exhibiting a VLASS detection.

4. OBSERVATIONS AND DATA ANALYSIS

4.1. VLA Observations

High sensitivity radio observations of all 18 targets were made with the VLA at S-band (2-4 GHz, central frequency 3 GHz), and X-band (8-12 GHz, central frequency 10 GHz), with the telescope in A configuration, and a channel width of 2 MHz. This provides a resolution of $0.65''$ at S-band and $0.2''$ at X-band (Project Code 22A-384, PI Schwartzman). The observations reach a sensitivity of $18.1 \mu\text{Jy}/\text{beam}$ at S-band, with a maximum recoverable scale of 18 arcseconds, and a sensitivity of $8.9 \mu\text{Jy}/\text{beam}$ at X-band, with a maximum recoverable scale of 5 arcseconds. Table 2 lists the observational details for each target, including the primary flux and phase calibrators, and synthesized beams. X-band targets were observed in repeated phase calibrator-target cycles, with a total on-source integration time of about 350 seconds per target, while S-band targets were observed in repeated phase calibrator-target-phase calibrator cycles, with a total on-source integration time of about 450 seconds per target.

4.2. Data Reduction

At S-band, the data were recorded with 16 spectral windows, each having 64 channels, and covering the 2-4 GHz band. For the X-band, the data were recorded with 48 spectral windows, each having 64 channels, and covering the 8-12 GHz band. The data were reduced and calibrated with the National Radio Astronomy Observatory’s (NRAO) Common Astronomy Software Applications (CASA; CASA Team et al. 2022) VLA Pipeline 1.4.2, using CASA version 5.3.0.

The initial pipeline steps followed standard procedures; the data were Hanning smoothed, antenna position corrections were applied, in addition to ionospheric TEC corrections and requantizer gains. Calibration was performed similarly, using antenna delay, bandpass, and gain solutions. The flux densities for the primary calibrations were taken from the Perley & Butler (2017) extension to the Baars et al. (1977) scale. The gain solutions were then transferred to the target sources.

Once pipeline calibration was completed, radio frequency interference (RFI) was removed where necessary using a combination of the CASA tasks `RFlag` and `TFCrop`. To refine the gain calibration, several rounds of self-calibration were performed where allowed (limited by low signal-to-noise in certain targets), beginning with phase-only, and proceeding to amplitude and phase where possible. All imaging was completed with CASA, and was performed with a multi-term multi-frequency

Table 1. Parameter Details

Parameter	Unit	Requirement	Meaning
(1)	(2)	(3)	(4)
<code>astrometric_excess_noise_sig</code>		≥ 5	identify targets with significant AEN
<i>Gaia</i> G magnitude	mag	< 20	mitigate spurious high-AEN targets near <i>Gaia</i> 's sensitivity limit
Redshift		> 0.5	eliminate targets with extended host galaxies
VCLASS Detection			identify targets with radio signatures

Table 1. Note - Column 1: Parameter used in target selection. Column 2: Parameter unit. Column 3: Parameter constraint used to define target sample. Column 4: Requirement for constraint used to define target sample.

synthesis (MTMFS) deconvolver (Rau & Cornwell 2011) and Briggs weighting, with a robust parameter of 0.5. Two Taylor terms were used to model the frequency dependence of the sky, and to account for the VLA's wide-band receivers. When necessary, W-projection with 64 w-planes (Cornwell et al. 2005; Cornwell 2008) was employed to account for the wide-field errors. Clean masks were employed at all stages.

4.3. Flux Measurements

Fluxes were measured with the Python Blob Detection and Source Finder package (PyBDSF; Mohan & Rafferty 2015). Every source in an image was fitted with a Gaussian, and the flux properties were recorded. All unresolved, point-like sources were fitted with a single Gaussian. For extended sources, a multi-Gaussian source was fitted. In some cases, for a cluster of closely associated peaks within an island (sources with multiple components), a single-Gaussian source was fitted to each peak.

Flux density scale errors were also taken into account. Following the VLA Observing Guide, a flux density scale calibration accuracy of 5% was assumed for both bands. Flux calibrators 3C48 and 3C138 are currently undergoing flares. While the 3C138 flare does not appear to impact measurements at the observed bands, the single target observed with 3C48 as a flux calibrator was assumed to have a flux density scale calibration accuracy of 10%.

5. SAMPLE PROPERTIES

We present new VLA observations of 18 quasars with significantly high astrometric excess noise. Targets were initially categorized by radio morphology, though we stress that morphology is not necessarily equivalent to the driver of the astrometric variability. An unresolved source features a single source that remains unresolved at sub-arcsecond scales. A resolved source features some structure at sub-arcsecond scales, and those targets have been further categorized as multi-component or extended targets. A more detailed discussion of each

category follows, as well as a more in-depth look at each individual target.

5.1. Unresolved Targets

Nine of the 18 targets display an unresolved point-like morphology at scales probed with the new VLA observations. Four of these are further identified as star+quasar superposition via an analysis of the SDSS spectra (see Section 7.1). Table 4 presents the properties of these nine targets, including fluxes, luminosities, and source angular and projected physical size, which is equivalent to an upper limit on the separation of any possible components.

While unresolved at sub-arcsecond scales, these sources may each be hiding more detailed structure at smaller scales. Upper and lower limits on the separation of any possible components were calculated from the new VLA observations and the varstrometry method respectively. As these sources are unresolved at sub-arcsecond scales, we may calculate an upper limit on their separation as the full extent of the unresolved source. As described in Section 2, AEN can be used, in combination with other quasar properties, to calculate a lower limit on the separation of any possible components.

While we may place constraints on these targets, without smaller-scale very long baseline interferometry (VLBI) observations, the astrometric driver of each system will likely remain uncharacterized. Some unresolved targets will likely be single AGN with a slightly increased intrinsic variability driving the AEN. Others, with follow-up observations, may be identified as quasar pair systems with separations that are not resolvable at these current scales. It is also possible for these sources to exhibit a variety of sub-milliarcsecond scale structure (i.e. jets or other extended emission associated with a single AGN) that is similarly unresolved. All of these possibilities could give rise to astrometric variability. Higher angular resolution follow-up will be required in order to confirm the morphology of these sources.

Table 2. Target Details

Source	Redshift	Scale	G	σ_{astro}	AENS	D_{pred}
[SDSS]		[kpc/arcsec]	[mag]	[mas]		[arcsec(kpcs)]
(1)	(2)	(3)	(4)	(5)	(6)	(7)
J011114.41+171328.5	2.198	8.47	19.29	4.46	42.27	0.08(0.73)
J024131.89-053139.6	0.837	7.84	17.51	1.51	37.58	0.03(0.23)
J074922.97+225511.8	2.166	8.49	18.52	1.48	12.82	0.02(0.25)
J080009.98+165509.4	0.708	7.39	18.30	4.51	175.2	0.09(0.64)
J081830.46+060138.0	2.381	8.35	17.80	0.66	5.220	0.01(0.11)
J095031.63+432908.4	1.771	8.67	17.90	3.27	139.7	0.06(0.55)
J095122.57+263513.9	1.247	8.56	17.48	1.65	76.31	0.03(0.27)
J104406.33+295900.9	2.983	7.90	18.88	1.61	10.08	0.03(0.25)
J105811.94+345808.7	1.061	8.34	18.21	0.83	5.200	0.01(0.14)
J112818.49+240217.4	1.607	8.69	18.53	1.09	5.506	0.02(0.19)
J121544.36+452912.7	1.132	8.44	19.09	1.22	5.411	0.02(0.20)
J141546.24+112943.4	2.519	8.26	17.56	8.03	1048.	0.16(1.29)
J143333.02+484227.7	1.357	8.64	19.08	1.94	13.20	0.03(0.33)
J155859.13+282429.3	2.300	8.41	19.04	2.92	35.05	0.05(0.48)
J162501.98+430931.6	1.653	8.69	19.23	8.20	156.9	0.16(1.39)
J172308.14+524455.5	2.568	8.22	17.72	0.64	6.503	0.01(0.11)
J173330.80+552030.9	1.201	8.52	18.58	1.73	17.27	0.03(0.29)
J210947.09+065634.7	2.939	7.93	19.49	10.2	195.8	0.20(1.60)

Table 2. Note - Column 1: Coordinate names in the form of “hhmmss.ss±ddmmss.s” based on SDSS DR16Q. Column 2: Spectroscopic redshift from SDSSDR16Q (Lyke et al. 2020), described in detail in Bolton et al. (2012). Column 3: Cosmological scale in kiloparsecs per arcsecond. Column 4: *Gaia* G-band mean magnitude. Column 5: *Gaia* astrometric_excess_noise. Column 6: *Gaia* astrometric_excess_noise_significance. Column 7: Predicted angular separation calculated assuming a typical fractional rms of 10%, which gives a predicted angular separation is $0.2''$ for every 10 milliarcseconds of σ_{astro} .

5.2. Resolved Targets

Nine of the 18 original targets display a resolved morphology. This is defined as any source with two or more clear radio peaks at either 3 GHz, 10 GHz, or both, or otherwise extended or complex emission. In order to help sort out targets which display a morphology consistent with that of an AGN pair, this category can be further subdivided into multi-component and extended/complex targets, both of which are discussed below.

5.2.1. Multi-component Targets

Six of the nine resolved targets have been identified as multi-component targets, defined as any source with two or more clear radio peaks at either 3 GHz, 10 GHz, or both. Table 5 presents the properties of these targets, including fluxes, luminosities, and angular and projected physical separations of the components at 10 GHz (with the exception of J1128+2402 (see Figure 10) for which

the separation was measured at 3 GHz due to the lack of a secondary radio peak in the 10 GHz observations).

Fluxes of the multi-component targets were measured as integrated fluxes. Given the lower resolution of the 3 GHz observations, some targets with resolved components at 10 GHz remain unresolved at 3 GHz. In those cases, the total flux of the 3 GHz signature has been reported, while the fluxes of each component at 10 GHz have been separately reported.

Our multi-component targets range in angular separation from 0.33 – 1.11 arcseconds, and in physical separation from 2.86 – 9.50 kiloparsecs, at redshifts of 1.247 to 2.166. While further analysis is still necessary, this range of separations at these redshifts is a parameter space that represents an observational gap in the known population of AGN pair systems (Chen et al. 2022a; Pfeifle 2023), and thus is of great interest.

Given the breadth of the definition used for multi-component targets, it is expected that the majority of

Table 3. Observation Details

Source	Obs. Date	Flux cal	Phase cal	$B_{maj} \times B_{min} \times PA$	$T_{int}(S)$	$T_{int}(X)$	σ_{3GHz}	σ_{10GHz}
[SDSS]	[UT]			[asec \times asec \times $^\circ$]	[s]	[s]	[μ Jy/bm]	[μ Jy/bm]
(1)	(2)	(3)	(4)	(5)	(6)	(7)	(8)	(9)
J011114.41+171328.5	29-03-2022	3C138	J0122+2502	$0.27 \times 0.21 \times 46$	318	436	22.7	17.6
J024131.89 - 053139.6	29-03-2022	3C138	J0239+0416	$0.19 \times 0.17 \times -72$	356	472	19.4	10.4
J074922.97+225511.8	21-03-2022	3C286	J0738+1742	$0.24 \times 0.17 \times -77$	328	474	20.5	9.40
J080009.98+165509.4	21-03-2022	3C286	J0738+1742	$0.23 \times 0.17 \times 49$	282	476	21.6	19.1
J081830.46+060138.0	21-03-2022	3C286	J0825+0309	$0.21 \times 0.18 \times -46$	358	416	20.2	11.2
J095031.63+432908.4	06-03-2022	3C147	J1018+3542	$0.21 \times 0.17 \times 53$	282	474	21.5	11.7
J095122.57+263513.9	06-03-2022	3C147	J0956+2515	$0.21 \times 0.17 \times 85$	323	474	19.7	9.30
J104406.33+295900.9	29-03-2022	3C147	J1018+3542	$0.18 \times 0.15 \times 20$	356	474	18.1	10.7
J105811.94+345808.7	29-03-2022	3C147	J1018+3542	$0.21 \times 0.16 \times 70$	358	476	19.4	10.1
J112818.49+240217.4	06-04-2022	3C286	J1125+2510	$0.25 \times 0.17 \times 86$	402	474	41.6	11.9
J121544.36+452912.7	06-04-2022	3C286	J1219+4829	$0.23 \times 0.16 \times 88$	338	476	20.1	9.30
J141546.24+112943.4	06-04-2022	3C286	J1415+1320	$0.19 \times 0.16 \times 23$	358	476	19.6	10.4
J143333.02+484227.7	06-04-2022	3C286	J1419+5423	$0.21 \times 0.17 \times -75$	328	476	18.7	8.90
J155859.13+282429.3	24-03-2022	3C286	J1613+3412	$0.31 \times 0.18 \times -62$	386	472	35.8	10.4
J162501.98+430931.6	24-03-2022	3C286	J1613+3412	$0.33 \times 0.18 \times 77$	328	446	72.1	19.1
J172308.14+524455.5	01-04-2022	3C286	J1740+5211	$0.28 \times 0.16 \times -77$	306	476	35.7	25.6
J173330.80+552030.9	01-04-2022	3C286	J1740+5211	$0.19 \times 0.17 \times 57$	298	476	28.2	14.8
J210947.09+065634.7	07-03-2022	3C48	J2123+0535	$0.26 \times 0.16 \times -81$	386	476	18.3	10.5

Table 3. Note - Column 1: Coordinate names in the form of “hhmmss.ss \pm ddmmss.s” based on SDSS DR16Q. Column 2: VLA observation date. Column 3: VLA flux calibrator. Column 4: VLA phase calibrator. Column 5: Restoring beam at 10 GHz: major axis, minor axis, position angle. Column 6: 3 GHz (S-band) VLA observation integration time. Column 7: 10 GHz (X-band) VLA observation integration time. Column 8: 1- σ sensitivity at 3 GHz, measured near the phase center. Column 9: 1- σ sensitivity at 10 GHz, measured near the phase center.

the sample will not be genuine dual quasar candidates. For example, J0951+2635 has been identified via spectroscopy as a gravitationally-lensed quasar (Schechter et al. 1998). However, with the currently available data, we calculate that 39% of the entire sample are targets identified as either lensed quasar systems or bonafide AGN pair systems. While the new VLA observations have directly observed the systems identified here as likely candidate dual quasar systems, follow-up observations (i.e. high angular resolution optical imaging and spectroscopy with *HST*, as targets lack any nearby reference stars necessary for adaptive optics) will be necessary to confirm the nature of these systems.

5.2.2. Extended and Complex Targets

Three of the 18 targets display jets or other extended emission more commonly associated with a single AGN, though multi-AGN systems are capable of exhibiting jet

activity (e.g. 3C75; Owen et al. 1985). This morphology generally provides an excellent indicator of the driver of the astrometric variability (Hwang et al. 2020). Table 6 presents the sample properties for the extended and jetted targets, including fluxes, luminosities, and the measured size of any extended emission on the sky.

Final fluxes were measured as discussed in Section 4.3. J1215+4529 features a pair of canonical radio jets. Table 6 presents the integrated fluxes of the core and both lobes, in addition to angular and projected physical sizes of the jet extensions and of the core. J1415+1129 and J1433+4842 both exhibit other forms of extended emission associated with the quasar. Given the complex nature of the targets, we have assigned four components, each coincident with a peak in the 10 GHz radio signature (see Figures 12 and 13), and measured the integrated flux for each. At 3 GHz, the integrated flux of the entire source was measured. Finally, the full extent on the sky of each target was measured (see Table 6).

Table 4. Sample Properties for Unresolved Sources

Source	S_{3GHz}	$\log(L_{3GHz})$	S_{10GHz}	$\log(L_{10GHz})$	$\Delta\theta_{r_p}$
[SDSS]	[mJy]	[WHz^{-1}]	[mJy]	[WHz^{-1}]	[arcsec(kpcs)]
(1)	(2)	(3)	(4)	(5)	(6)
J024131.89-053139.6†	0.57±0.025	24.26	0.15±0.02	23.68	1.13(8.86)
J080009.98+165509.4	1.81±0.03	24.62	2.23±0.04	24.95	0.28(2.07)
J081830.46+060138.0	0.28±0.02	25.08	0.061±0.01	24.42	0.27(2.25)
J104406.33+295900.9	156.5±0.08	28.06	125.8±0.09	27.97	0.31(2.45)
J105811.94+345808.7	0.32±0.03	24.35	0.069±0.03	23.68	0.24(2.00)
J155859.13+282429.3†	1.17±0.06	25.69	0.56±0.06	25.38	0.29(2.44)
J172308.14+524455.5†	1.06±0.018	25.39	2.91±0.01	25.83	0.27(2.22)
J173330.80+552030.9	7.03±0.03	25.78	4.68±0.01	25.61	0.28(2.39)
J210947.09+065634.7†	5.58±0.02	26.62	1.57±0.01	26.07	0.25(1.98)

Table 4. Note - Column 1: Coordinate names in the form of “hhmmss.ss±ddmmss.s” based on SDSS DR16Q; † indicates target identified as star+quasar superposition via SDSS spectrum. Column 2: VLA 3 GHz (S-band) peak flux ± error. Column 3: VLA 3 GHz (S-band) peak luminosity. Column 4: VLA 10 GHz (X-band) peak flux ± error. Column 5: VLA 10 GHz (X-band) peak luminosity. Column 6: Upper limit on AGN pair separation where applicable, reported in arcseconds and kiloparsecs, measured from angular width of unresolved source at 10 GHz.

6. RADIO SPECTRAL MODELING

We performed radio spectral modeling using data from a variety of public radio surveys (see Section 6.1. Radio spectral shapes, in combination with morphological information, reveal important information about the quasar environment, the physical conditions of the jets/lobes (e.g. absorbed vs. optically-thin), and the evolutionary stage of the radio source (Nyland et al. 2020; Bicknell et al. 1998; O’Dea 1998; O’Dea & Saikia 2021; Orienti & Dallacasa 2014).

The observed radio spectrum is a combination of absorption and emission processes. To quantify the distribution and the location of the spectral peak, least squares fitting was performed for the new VLA observations presented above, in addition to all available archival and commensal observations. Two basic synchrotron emission models were employed which will allow us to constrain important physical properties of each radio source.

- **Standard Power Law:** A standard power law model that is defined by $S_\nu = S_o\nu^\alpha$, where S_ν is the flux density at frequency ν , α is the spectral index, and S_o is the flux density at 1 GHz. The value and sign of the spectral index can be used to help distinguish between synchrotron and thermal emission (e.g., Patil et al. 2021, 2022).
- **Curved Power Law:** A curved power law represented by a parabola generated from the flux at

frequency ν , S_ν , the spectral index α , and the flux density at 1 GHz S_o , defined as $S_\nu = S_o\nu^\alpha e^{q(\ln\nu)^2}$, where q represents the width of the peak, characterizes the degree of curvature, and is defined as $\nu_{peak} = e^{-\alpha/2q}$, where ν_{peak} is the peak frequency. Significant spectral curvature is typically defined as $|q| \geq 0.2$ (Duffy & Blundell 2012). Absorption may be due to a high synchrotron optical depth within the source (i.e., synchrotron self-absorption (SSA); O’Dea & Saikia 2021) or free-free absorption from surrounding ionized gas (Bicknell et al. 1998). Understanding which process is in play can further constrain the radio source and environment properties.

Following the approach described in Patil et al. (2022), each source was fitted with a standard power law and a curved power law, making use of the **Radio Spectral Fitting**¹ tools (Patil et al. 2021). The new VLA data at 10 GHz were re-imaged and uv-tapered to produce similar resolutions in both the X- and S-bands. The uv-tapered image properties are described in Table 7. The results of the least squares fitting are summarized in Table 8, and the radio spectra are presented in Appendix D. Important results from the radio spectral modeling are included in Section 7.2.

6.1. Archival Radio Surveys

¹ https://github.com/paloween/Radio_Spectral_Fitting

Table 5. Sample Properties for Multi-component Sources

Source	S_{3GHz}	$\log(L_{3GHz})$	S_{10GHz}	$\log(L_{10GHz})$	$\Delta\theta(r_p)$	Class
Comp. coord.						
[SDSS]	[mJy]	[WHz^{-1}]	[mJy]	[WHz^{-1}]	[arcsec(kpcs)]	
(1)	(2)	(3)	(4)	(5)	(6)	(7)
J011114.41+171328.5*					0.94(7.96)	Multi
01:11:14.42 +17:13:28.58	77.0±0.23	27.46	66.8±0.16	27.41	-	NE
01:11:14.37 +17:13:27.96	1.76±0.09	25.82	3.36±0.14	26.11	-	SW
074922.97+225511.8*					0.46(3.91)	Multi
07:49:22.99 +22:55:12.02	104.9±0.19	27.55	17.5±0.16	26.77	-	NE
07:49:22.97 +22:55:11.76	-	-	48.7±0.09	27.22	-	SW
J095031.63+432908.4*					0.33(2.86)	Multi
09:50:31.63 +43:29:08.59	2.61±0.06	25.73	1.42±0.04	25.46	-	N
09:50:31.63 +43:29:08.26	-	-	0.44±0.02	24.95	-	S
J095122.57+263513.9*					1.11(9.50)	Lens
09:51:22.57 +26:35:14.03	0.57±0.04	24.69	0.81±0.02	24.85	-	NW
09:51:22.64 +26:35:13.41	0.19±0.04	24.22	0.23±0.02	24.29	-	SE
112818.49+240217.40*					0.72(6.26)	Multi
11:28:18.52 +24:02:17.73	0.12±0.03	24.32	0.14±0.03	24.39	-	NE
11:28:18.48 +24:02:17.33	0.075±0.02	24.12	-	-	-	SW
J162501.98+430931.6*					0.52(4.52)	Multi
16:25:01.99 +43:09:31.93	1.31±0.08	25.36	0.12±0.03	24.32	-	N
16:25:01.99 +43:09:31.39	-	-	0.41±0.03	24.86	-	S

Table 5. Note - Column 1: Coordinate names in the form of “hhmmss.ss±ddmmss.s” based on SDSS DR16Q are bolded and starred, and individual coordinate location as measured from 10 GHz VLA observations are listed beneath. Column 2: VLA 3 GHz (S-band) peak flux \pm error. Column 3: VLA 3 GHz (S-band) peak luminosity. Column 4: VLA 10 GHz (X-band) peak flux \pm error. Column 5: VLA 10 GHz (X-band) peak luminosity. Column 6: AGN pair separation where applicable, reported in arcseconds and kiloparsecs, measured at 10 GHz, with the exception of J1128+2402, for which the separation was measured at 3 GHz due to lack of a secondary peak in the 10 GHz observations. Column 7: Classification and component location.

Radio spectral modeling with broad frequency coverage required adding survey data to our new observations. Radio flux densities and their uncertainties were taken from the following archival surveys. The flux density values are taken directly from the published catalogs with corrections applied for calibration uncertainties.

6.1.1. LOTSS

The Low Frequency Array Two-meter Sky Survey (LOTSS; Shimwell et al. 2019, 2022) is an ongoing all-sky survey at 144 MHz covering the northern sky above 34 degrees. The second data release covers about 27% of the sky with a point-source sensitivity of 83 μ Jy per beam. A calibration uncertainty of 10% was applied.

6.1.2. TGSS ADR

The Tata Institute of Fundamental Research (TIFR) Giant Metrewave Radio Telescope (GMRT) Sky Survey Alternative Data Release (TGSS ADR; Intema et al. 2017) is a 150 MHz survey covering about 90% of the sky, or about 36900 deg². TGSS reaches a resolution of 25'', and has a 1σ sensitivity of between 3 and 5 mJy per beam. A calibration uncertainty of 10% was applied.

6.1.3. VLITE

The VLA Low-band Ionosphere and Transient Experiment (VLITE; Clarke et al. 2016; Polisensky et al. 2016) is a commensal system on the VLA operating at all configurations that records of 6000 hours of commensal data per year at 350 MHz. With the VLA in A configuration (as it was for all targets in this project), VLITE reaches a resolution of about 5.6''. A calibration uncertainty of 15% was applied.

Table 6. Sample Properties for Extended Sources

Source [SDSS]	Class	S_{3GHz} [mJy]	$\log(L_{3GHz})$ WHz^{-1}	S_{10GHz} [mJy]	$\log(L_{10GHz})$ WHz^{-1}	$\Delta\theta(r_p)$ [arcsec(kpcs)]
(1)	(2)	(3)	(4)	(5)	(6)	(7)
J121544.36+452912.7*	Jet					
12:15:44.36 +45:29:12.78	Core	23.4±0.05	26.21	16.4±0.03	26.06	0.25(2.11)
12:15:43.94 +45:29:20.20	N Lobe	1.38±0.13	24.98	0.57±0.06	24.59	8.80(74.27)
12:15:44.38 +45:29:05.12	S Lobe	4.61±0.16	25.51	0.708±0.09	24.69	11.53(97.31)
J141546.24+112943.4*	Lens					1.73(14.29)
14:15:46.24 +11:29:43.40	Unresolved	2.61±0.19	26.13	-	-	-
14:15:46.27 +11:29:43.81	A	-	-	0.31±0.03	25.21	-
14:15:46.28 +11:29:43.23	B	-	-	0.16±0.04	24.92	-
14:15:46.23 +11:29:43.13	C	-	-	0.21±0.04	25.04	-
14:15:46.19 +11:29:44.12	D	-	-	0.09±0.02	24.67	-
J143333.02+484227.7*	Jet					1.39(12.01)
14:33:33.02 +48:42:27.70	Unresolved	34.9±0.22	26.56	-	-	-
14:33:33.03 +48:42:27.76	A	-	-	1.1±0.07	25.06	-
14:33:32.99 +48:42:27.58	B	-	-	7.24±0.15	25.88	-
14:33:30.90 +48:42:27.56	C	-	-	1.64±0.09	25.24	-
14:33:32.89 +48:42:27.85	D	-	-	0.12±0.03	24.10	-

Table 6. Note - Column 1: Coordinate names in the form of “hhmmss.ss±ddmms.s” based on SDSS DR16Q are bolded and starred, and individual component locations as measured from new 10 GHz VLA observations are listed beneath. Column 2: Classification and component label. Column 3: VLA 3 GHz (S-band) peak flux ± error. Column 4: VLA 3 GHz (S-band) peak luminosity. Column 5: VLA 10 GHz (X-band) peak flux ± error. Column 6: VLA 10 GHz (X-band) peak luminosity. Column 7: AGN pair separation where applicable, reported in arcseconds and kiloparsecs, measured from 10 GHz observations.

6.1.4. RACS

The Rapid Australian Square Kilometer Array Pathfinder (ASKAP) Continuum Survey (RACS; [McConnell et al. 2020](#)) is the first all-sky survey conducted with ASKAP. The first epoch observations at 887.5 MHz use 36 12-m antennas to cover the entire sky south of +41 degrees, reaching a sensitivity of between 25 and 40 μ Jy per beam and a beam of about 15". A calibration uncertainty of 5% was applied.

6.1.5. NVSS

The NRAO VLA Sky Survey (NVSS; [Condon et al. 1998](#)) observed the entire northern sky about $\delta > -40$ degrees at 1.4 GHz. The survey was conducted with the VLA in D configuration, resulting in an angular resolution of about 45". A calibration uncertainty of 3% was applied.

6.1.6. FIRST

The Faint Images of the Radio Sky at Twenty-one centimeters (FIRST; [Becker et al. 1995](#)) survey is a 1.4

GHz survey covering 10,575 deg² of the sky. The observations reach a resolution of about 5" and a sensitivity of ~ 15 mJy per beam. A calibration uncertainty of 5% was applied.

6.1.7. VLASS

The VLA Sky Survey (VLASS; [Lacy et al. 2019](#)) is an ongoing 3 GHz continuum survey covering 33,885 deg². Of the 3 planned epochs, the first two have been completed, and the third is ongoing. A source catalog² is now available ([Gordon et al. 2021](#)). The typical 1σ sensitivity of a single epoch image is ~ 120 μ Jy per beam with an angular resolution of 2.5". A calibration uncertainty of 3% was applied.

6.1.8. VIPS

The VLBA Imaging and Polarimetry Survey (VIPS; [Helmboldt et al. 2007](#)) observed 1128 flat-spectrum

² Quick-look image cutouts are also available at the Canadian Institute for Radio Astronomy Data Analysis: <http://cutouts.cirada.ca/>

sources brighter than 85 mJy in the Northern Cap region of SDSS at 5 GHz, covering about 14% of the sky. The typical 1σ sensitivity of a VIPS image is ~ 0.2 mJy per beam with an angular resolution of 1.4 milliarcseconds. A calibration uncertainty of 5% was applied.

7. DISCUSSION

7.1. *Chance Superposition with Stars*

One possible alternative explanation for both the dual component and the unresolved targets is star+quasar superposition. To assess this possibility, we retrieved the SDSS spectra for the targets in this sample and searched the spectra for $z = 0$ absorption lines using Bayesian AGN Decomposition Analysis for SDSS Spectra (BADASS; Sexton et al. 2021) package.³ BADASS is an open-source spectral analysis program designed for deconvolution of AGN and host galaxy spectra via simultaneous fitting for a variety of spectral features, including but not limited to: the AGN power law continuum, individual broad, narrow, and absorption lines, and stellar host templates or (alternatively) the stellar line-of-sight velocity distribution.

For each target in the sample, we began by fitting host stellar population templates to the observed SDSS spectrum around common $z = 0$ stellar absorption features (Ca triplet, CaT, rest-frame 8500 Å, 8544 Å, and 8664 Å; Ca H+K lines, rest-frame 3934 Å and 3969 Å; NaD, rest-frame 5890 Å and 5896 Å, MgIb wavelength; H α , rest-frame 6563 Å; H β , rest-frame 4861 Å). We did not incorporate any fitting of emission or absorption lines or the quasar continuum during these initial ‘quick-look’ fits. Each fit was then visually inspected for signs of absorption lines. In cases where absorption lines were identified, we swapped the host stellar template for an AGN power law continuum (to the model the background quasar continuum) and included narrow absorption lines to the fit of the observed spectrum; we centered these absorption lines on the expected $z = 0$ rest-frame wavelengths of the lines (see above), left their amplitudes free to vary, and then refit the spectrum.

Through this iterative fitting process, we found evidence for CaT in J155859.13+282429.3, J172308.14+524455.5, and J210947.09+065634.7, NaD lines in J024131.89-053139.6, J155859.13+282429.3, J172308.14+524455.5, and J210947.09+065634.7, and H α in J172308.14+524455.5, but we do not find evidence for MgIb, H β , or Ca H+K lines in any targets. The lack of evidence for MgIb and Ca H+K lines is not particularly surprising; the rest-frame wavelengths

for the Ca H+K lines reside in a spectral region of low throughput in SDSS while MgIb is not a particularly strong line relative to other lines. Figure 3 displays examples of our absorption line fits to the CaT lines in J155859.13+282429.3, J172308.14+524455.5, and J210947.09+065634.7 and the NaD lines in J024131.89-053139.6, along with inset panels showing the full SDSS spectra. These results demonstrate that 4 systems in this sample comprise quasar-star pairs caught in projection. Assuming no other systems within this sample comprise quasar-star pairs, our sample has a quasar-star contamination rate of $24.2^{+10.4}_{-8.7}\%$ (estimated using SCIPY.SPECIAL.BETAINCINV). However, the absence of foreground stellar absorption lines does not necessarily preclude the presence of other quasar-star pairs within this sample; it has been shown even in the local Universe that the continuum of background AGNs can easily dominate the stellar continuum of foreground stars (even when the sources are separated by $\sim 6''$, Pfeifle et al. 2023), and foreground, $z = 0$ stellar absorption features can be either diluted or completely elusive. Our quasar-star pair contamination rate is therefore a lower limit for this sample.

7.2. *Individual Targets*

In this section, we present a more in-depth study of the existing ancillary multi-frequency data that exists for each target in the sample, in conjunction with the new VLA observations and SDSS spectra analysis. Final radio images are presented in Appendix A.

SDSS011114.41+171328.5: exhibits multiple bright components in both radio bands, with a separation of 0.94 arcseconds, or 7.96 kiloparsecs. We identify this target as a candidate dual AGN.

SDSS024131.89-053139.6: is an unresolved point source at sub-arcsecond scales, with perhaps some slight extension to the NE. The SDSS spectrum for this target reveals evidence of a $z = 0$ stellar absorption Na doublet, and has thus been identified as a star+quasar superposition.

SDSS074922.97+225511.8: exhibits two radio peaks in both VLA bands, with a separation of 0.46 arcseconds, or 3.91 kiloparsecs. It is another candidate dual AGN, and has been previously identified as such by Chen et al. (2022a), with dual-band *HST* observations (see Figure 5; middle), in addition to Gemini GMOS spectra. Shen (2021) reported a separation of 3.8 kiloparsecs, essentially matching the separation measured from the new VLA observations. Finally, Shen (2021) reports initial follow-up VLBA observations that confirm the existence of and indicate morphological differences in the dual cores.

SDSS095031.63+432908.4: exhibits a single, ex-

³ <https://github.com/remingtonsexton/BADASS3>

Table 7. Tapered Image Properties

Source	$B_{maj} \times B_{min} \times PA$	S_{10GHz}	σ_{10GHz}
[SDSS]	[asec \times asec \times $^\circ$]	[mJy]	[$\mu Jy/bm$]
(1)	(2)	(3)	(4)
J011114.41+171328.5	$0.84 \times 0.60 \times 81$	70.80 ± 0.22	59.3
J024131.89 - 053139.6	$0.71 \times 0.60 \times 48$	0.18 ± 0.05	24.7
J074922.97+225511.8	$0.66 \times 0.57 \times 66$	66.40 ± 0.16	32.4
J080009.98+165509.4	$0.67 \times 0.58 \times 70$	2.23 ± 0.06	22.2
J081830.46+060138.0	$0.69 \times 0.58 \times 67$	0.12 ± 0.04	15.8
J095031.63+432908.4	$0.69 \times 0.61 \times -67$	1.79 ± 0.05	15.2
J095122.57+263513.9	$0.72 \times 0.59 \times -69$	1.08 ± 0.04	13.8
J104406.33+295900.9	$0.81 \times 0.55 \times 82$	128.1 ± 0.24	65.2
J105811.94+345808.7	$0.76 \times 0.55 \times -84$	0.07 ± 0.02	15.2
J112818.49+240217.4	$0.67 \times 0.59 \times 78$	0.13 ± 0.04	15.7
J121544.36+452912.7	$0.66 \times 0.58 \times 73$	16.40 ± 0.06	25.3
J141546.24+112943.4	$0.79 \times 0.59 \times -85$	0.99 ± 0.15	14.1
J143333.02+484227.7	$0.71 \times 0.59 \times 86$	14.11 ± 0.44	35.4
J155859.13+282429.3	$0.74 \times 0.56 \times -88$	0.71 ± 0.03	13.7
J162501.98+430931.6	$0.71 \times 0.58 \times 88$	0.63 ± 0.05	14.5
J172308.14+524455.5	$0.66 \times 0.59 \times 41$	3.01 ± 0.03	16.1
J173330.80+552030.9	$0.66 \times 0.59 \times 43$	4.71 ± 0.03	15.5
J210947.09+065634.7	$0.73 \times 0.58 \times 82$	1.57 ± 0.04	17.6

Table 7. Note - Column 1: Coordinate names in the form of “hhmmss.ss \pm ddmmss.s” based on SDSS DR16Q. Column 2: Restoring beam of uv-tapered imaging: major axis, minor axis, position angle. All imaging done with Briggs weighting and a robust factor of 1. Column 3: 10 GHz uv-tapered image source flux \pm error. Column 4: 10 GHz uv-tapered image 1- σ noise.

tended radio source at 3 GHz that resolves into two component peaks at 10 GHz, with a separation of 0.34 arcseconds, or 2.86 kiloparsecs. We identify this target as another candidate dual AGN. The radio spectrum for this target is curved, with a peak frequency of 0.37 GHz, and a curved spectral index of 0.44.

SDSS095122.57+263513.9: exhibits two radio peaks at both VLA bands. It has been identified as a lensed quasar via spectroscopy (Schechter et al. 1998) and followed-up by the Gravitational Lenses and Dark Matter project (GLENDAMA; Gil-Merino et al. 2018; Sluse et al. 2012). Follow-up HST (Jakobsson et al. 2005) observations confirm that this system comprises a lensed quasar with a separation of 1.11 arcseconds (see Figure 5; right). The radio spectrum for this target is curved and inverted. It exhibits a lowest flux at 4.56 GHz, and a curved spectral index of -2.45.

SDSS104406.33+295900.9: is an unresolved point

source at sub-arcsecond scales. It is bright in both bands, and has previous VLBA observations from the VLBA Imaging and Polarimetry Sky Survey at 5 GHz (VIPS; Helmboldt et al. 2007). Figure 4 shows the archival VLBA image, displaying a bright radio source still consistent with an unresolved point source at milliarcsecond scales. The radio spectrum for this target is likely curved, though there are archival fluxes significantly offset from the model that might indicate flux variability over years-long timescales. Recently, Wang et al. (2023) found, from new e-MERLIN observations of this target, a significant and large *Gaia*-radio offset.

SDSS112818.49+240217.4: exhibits two radio peaks at 3 GHz. The eastern peak is not visible at 10 GHz, leaving only the western peak remaining. We identify this target as a possible dual AGN, with a separation of 0.72 arcseconds, or 6.26 kiloparsecs.

SDSS121544.36+452912.7: features a pair of canoni-

Table 8. Radio Spectral Modeling Properties

Source	S_{3GHz}	S_{10GHz}	α_{Power}	α_{Curved}	Class
[SDSS]	[mJy]	[mJy]			
(1)	(2)	(3)	(4)	(5)	(6)
J011114.41+171328.5	78.7 ± 0.24	70.8 ± 0.22	-0.09 ± 0.01	-0.30 ± 0.06	Multi Component
J024131.89 - 053139.6	0.63 ± 0.05	0.18 ± 0.05	-1.09 ± 0.09	-1.33 ± 0.01	Star+quasar
J074922.97+225511.8	104 ± 0.19	66.4 ± 0.16	-0.37 ± 0.02	0.14 ± 0.21	Multi Component
J080009.98+165509.4	1.89 ± 0.04	2.23 ± 0.06	0.04 ± 0.15	-1.46 ± 0.47	Unresolved
J081830.46+060138.0	0.31 ± 0.04	0.12 ± 0.04	-1.93 ± 0.47	-3.01 ± 0.01	Unresolved
J095031.63+432908.4	2.61 ± 0.06	1.79 ± 0.05	0.08 ± 0.17	0.44 ± 0.07	Multi Component
J095122.57+263513.9	0.76 ± 0.06	1.08 ± 0.04	0.07 ± 0.38	-2.45 ± 0.01	Lens
J104406.33+295900.9	156 ± 0.24	128 ± 0.24	-0.06 ± 0.08	3.09 ± 0.45	Unresolved
J105811.94+345808.7	0.32 ± 0.03	0.07 ± 0.02	-0.94 ± 0.05	-0.97 ± 0.01	Unresolved
J112818.49+240217.4	0.26 ± 0.04	0.13 ± 0.04	-0.58 ± 0.15	- ± -	Multi Component
J121544.36+452912.7	23.4 ± 0.05	16.4 ± 0.06	-0.30 ± 0.04	-0.72 ± 0.08	Jet
J141546.24+112943.4	2.61 ± 0.18	0.99 ± 0.15	-1.13 ± 0.09	-1.18 ± 0.15	Lens
J143333.02+484227.7	34.9 ± 0.22	14.1 ± 0.44	-0.86 ± 0.11	-0.88 ± 0.14	Jet
J155859.13+282429.3	1.27 ± 0.04	0.71 ± 0.03	-0.58 ± 0.19	-1.14 ± 0.23	Star+quasar
J162501.98+430931.6	1.31 ± 0.08	0.63 ± 0.05	-0.89 ± 0.08	-0.94 ± 0.06	Multi Component
J172308.14+524455.5	1.11 ± 0.03	3.01 ± 0.03	0.83 ± 0.01	- ± -	Star+quasar
J173330.80+552030.9	7.01 ± 0.03	4.71 ± 0.03	-0.33 ± 0.03	-0.69 ± 0.26	Unresolved
J210947.09+065634.7	5.58 ± 0.04	1.57 ± 0.04	-0.91 ± 0.15	0.46 ± 0.29	Star+quasar

Table 8. Note - Column 1: Coordinate names in the form of “hhmmss.ss±ddmmss.s” based on SDSS DR16Q. Column 2: VLA 3 GHz (S-band) total flux ± error. Column 3: VLA 10 GHz (X-band) uv-tapered total flux ± error. Column 4: Spectral index from least squares fitting of radio spectral fitting with standard power law ± error. Column 5: Spectral index from least squares fitting of radio spectral fitting with curved power law ± error, where possible. Column 6: Classification.

cal radio jets, between which exists a compact core. The northern jet is diffuse, with a separation from the core of 8.80 arcseconds, or about 74 kiloparsecs. The southern jet exhibits a knot at 7.55 arcseconds from the core, or about 64 kiloparsecs, and then continues on to a diffuse lobe at 11.53 arcseconds, or about 97 kiloparsecs.

SDSS141546.24+112943.4: is an unresolved point source at 3 GHz that resolves into at least four individual components at 10 GHz. The end-to-end extension of the target is 1.73 arcseconds, or about 14 kiloparsecs. Archival *HST* images reveal that the target is a lensed quasar (see Figure 5; left); an Einstein Cross known colloquially as the Cloverleaf System (Chartas et al. 2004).

SDSS143333.02+484227.7: exhibits a jet-like extension to the west of the radio core, and a smaller extension to the east. The extension is relatively small-scale: measured from end-to-end, the full length of the tar-

get is 1.39 arcseconds, or about 12 kiloparsecs. For this target, there is a secondary faint (magnitude of ~ 21) *Gaia* detection close to the primary source ($\sim 0.767''$). The secondary source is $\sim 18\%$ of the brightness of the primary source.

SDSS155859.13+282429.3: is an unresolved point source in both bands. The SDSS spectrum for this target reveals evidence for both a Ca triplet and a Na doublet absorption system, and has thus been identified as a star+quasar superposition. This target is the most obvious star-quasar pair; the SDSS spectrum also exhibits prominent TiO absorption bands, which are a common characteristic of M dwarfs (Morgan et al. 1943).

SDSS162501.98+430931.6: exhibits a single, extended radio source at 3 GHz, that resolves into two radio components at 10 GHz. This target is another

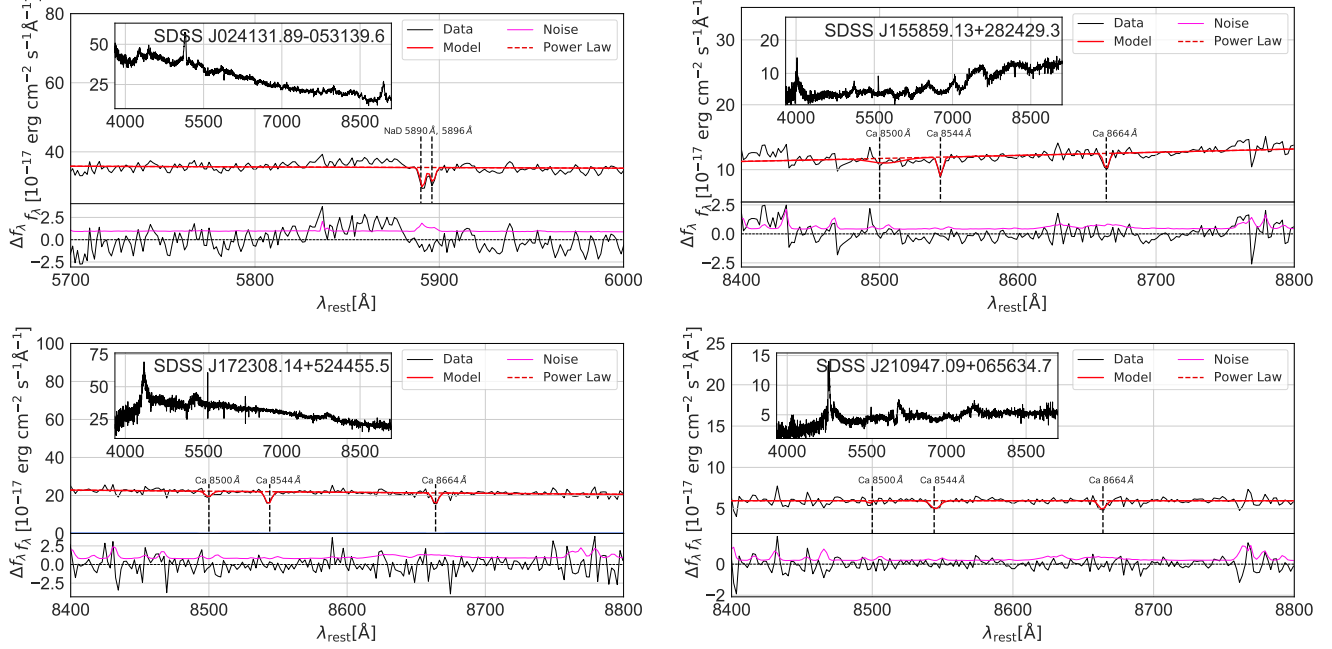


Figure 3. SDSS optical spectroscopic absorption line fitting. Here we show the four cases of confirmed foreground star-background quasar pairings (top: J0241-0531, top-middle: J1558+2824, bottom-middle: J1723+5244, bottom: J2109+0656) where we have identified foreground stellar absorption features consistent with $z = 0$. Each panel shows (1) the fits to the spectrum across a narrow spectral window straddling the observed absorption lines, (2) the residuals of the fit, and (3) an inset panel showing the full SDSS spectrum. Black lines represent the observed SDSS spectrum (uncorrected for the redshift of the quasar), red lines represent the model (quasar power-law continuum + gaussian absorption lines). We have marked the observed absorption lines with dashed vertical lines and denoted the specific line by name. The full SDSS spectra for these four likely star-quasar pairs are shown in Appendix 9 along with the SDSS spectra of the rest of the sample.

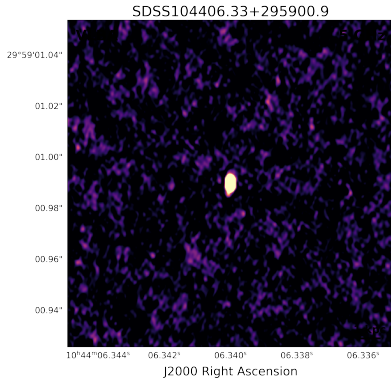


Figure 4. VIPS 5 GHz VLBA observations of SDSS104406.33+295900.9 with a $0.0029'' \times 0.0018''$ beam.

candidate dual AGN, with a separation of 0.52 arcseconds, or 4.52 kiloparsecs.

SDSS172308.14+524455.5: is an unresolved point source at sub-arcsecond scales, with no clear extension in the fairly bright radio signature. The SDSS spectrum for this target reveals evidence for a $z = 0$ Ca triplet,

Na doublet, and H α absorption lines, and has thus been identified as a star+quasar superposition.

SDSS210947.09+065634.7: is an unresolved point source at sub-arcsecond scales. The SDSS spectrum for this target reveals evidence of a $z = 0$ Na doublet and a Ca triplet absorption line system, and has thus been identified as a star+quasar superposition. The radio spectrum for this target is curved, with a peak frequency of 1.67 GHz and a curved spectral index of 0.46. Recently, Wang et al. (2023) found, from new e-MERLIN observations of this target, a significant and large *Gaia*-radio offset.

7.3. Dual Quasars versus Lensed Quasars

One of the primary goals of this study is to identify candidate dual AGN systems. For the portion of the sample identified as multi component targets, it is necessary to eliminate both star+quasar superpositions and lensed quasars contaminants. After eliminating foreground stellar contaminants, Shen (2021) argued that the abundance of high-redshift sub-arcsecond gravitationally lensed quasars is insufficient to account for most of the resolved pairs in a systematic search. This indicates that, while we can expect some additional lensed interlopers, the majority of our remaining sample will be bona fide AGN pairs.

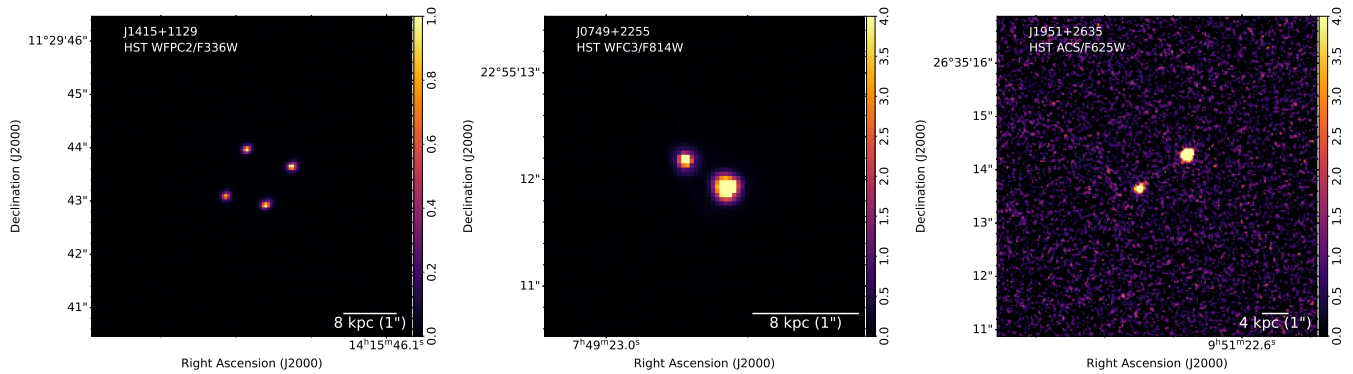


Figure 5. Left: HST WFPC2/F336W observations of SDSS141546.24+112943.4, illustrating the lensed quasar, an Einstein Cross known as the Cloverleaf System (Chartas et al. 2004). Middle: HST WFC3/F814W observations of SDSSJ074922.97+225511.8, illustrating a likely AGN pair. Right: HST ACS/F625W observations of SDSS095122.57+263513.9, illustrating a known gravitationally-lensed quasar (Schechter et al. 1998).

Two targets in the pilot sample have been identified as lensed quasars (J1415+1129; see Figure 5; left, and J0951+2635; see Figure 5; right). In J1415+1129, the unresolved but extended source at 3 GHz resolves into at least four individual components at 10 GHz. Archival HST observations reveal that the target is a lensed quasar, an Einstein Cross type system known colloquially as the Cloverleaf System (Chartas et al. 2004). Interestingly, the radio and optical peaks are not aligned, as was similarly observed at 8.4 GHz (Kayser et al. 1990), where an offset between the optical and modeled radio centroid was measured. However, CO(7-6) observations display good spatial alignment (Alloin et al. 1997) and a recent multi-wavelength study reports the discovery of a radio lobe (Zhang et al. 2022).

In J0951+2635, the double lens is resolved at both new radio frequencies. Archival HST observations reveal a similar optical structure. The target was identified as a lensed quasar via spectroscopy (Schechter et al. 1998), and followed-up by the GLENDAMA (Gil-Merino et al. 2018) and COSMOGRAIL (Sluse et al. 2012) projects. Finally, follow-up HST observations (Jakobsson et al. 2005) confirm the identification.

For the other multi-component targets, a lens cannot be ruled out. One possible avenue of further investigation would be follow-up high-resolution integral-field (IFU) spectroscopy of both peaks (Rusu et al. 2019; Lemon et al. 2018). While a nearly identical spectrum does not necessarily preclude a dual AGN morphology (given the general similarity of quasar spectra), similar changes in luminosity over time (requiring multi-epoch IFU) might be indicative of a lensed system (e.g. Ciurlo et al. 2023; Lemon et al. 2020, 2023). Another method might be to search for possible lensing galaxies in deeper, high angular resolution imaging of these systems (Lemon et al. 2018; Lemon et al. 2023).

7.4. Understanding the Varstrometry-selected Radio Parameters

In addition to understanding each individual source, it is equally important to understand the sample that the **varstrometry** method selects for. In order to characterize the overall target sample, a control sample was prepared. The control sample was generated alongside the target sample, and systems identified as star+quasar superpositions were identified by their SDSS spectra and were eliminated from the target sample.

The control sample was generated from a cross-match of the SDSS DR16Q and *Gaia* EDR3 catalogs, to within $1.5''$. The sample *Gaia* G-magnitude ($G < 20$) and redshift ($z > 0.5$) cuts were applied. In this case, the important *Gaia* parameter, the **astrometric_excess_noise_significance** was set to < 4 , in order to generate a control sample of sources that do not display significant astrometric jitter. Finally, it was required that each control source have a VLASS signature so that overall control and target sample radio parameters could be compared. The control sample was then spatially matched to the target sample, so as to ensure that the controls covered the same portion of the sky as the targets to minimize systematics arising from the *Gaia* scanning law. The number of controls per target object was maximized and required to be the same for each target. Additionally, no controls were shared between targets, resulting in a control sample of about 120 sources.

The controlled parameters, *Gaia* G-magnitude and redshift, show probability values calculated using the Anderson-Darling, Kolmogorov-Smirnov, and Kuiper’s tests that are > 0.05 , indicating that the null hypothesis (in this case, that both the target and control samples arise from the same parent population) cannot be ruled out. The same is true for the *Gaia* G-magnitude signal-to-noise ratio, the peak radio luminosities, the total radio luminosities, the ratio of peak-to-total radio luminosity, and radio spectral indices. For the controlled parameter AENS, the p-values are < 0.05 , rejecting the null hypothesis, and indicating that the two samples vary by more than the parameter of interest.

Distributions are shown in Figure 6, illustrating the offset in the AENS. The controlled parameters exhibit the relationship driven by the sample selection parameters, but the important radio parameters (peak radio luminosity, total radio luminosity, ratio of peak-to-total radio luminosity, and radio spectral index) illustrate that the target sample is not radio-loud when compared to the matched control sample, likely eliminating the possibility of blazar jet activity driving a large percentage of the high AEN.

8. SUMMARY AND CONCLUSIONS

We present deep, targeted VLA observations of 18 *Gaia*-unresolved quasars identified as astrometrically-variable. The high redshifts ($0.8 \leq z \leq 2.9$) of these quasars probe an interesting observational gap in the current population of confirmed and candidate kiloparsec-scale dual AGN near cosmic noon. This pilot study, which combines the varstrometry method (Hwang et al. 2020) with high-resolution radio observations, is the first in a series of studies designed to fully understand the radio+varstrometry sample. Our conclusions are as follows:

- The new VLA observations reveal six multi-component targets, or $\sim 39\%$ of the overall sample. This includes J0951+2635, which has been identified as a lensed quasar. Optical/infrared spectroscopy and imaging will be required to filter out other contaminants by identifying stellar features, modeling lensed quasar systems, and identifying lensing galaxies.
- Three of the 18 targets have been identified as systems exhibiting jet activity or otherwise extended emission. This population includes J1415+1129, which has been identified from existing HST observations as a lensed quasar.
- Nine of the 18 targets have unresolved radio signatures. After careful analysis of the SDSS spectra, four of these nine were identified as superpositions of foreground stars and background quasars, and thus were eliminated as candidate dual AGN. There remain many astrophysical explanations for the excess astrometric noise exhibited by these targets. Follow-up multiwavelength observations will be required to observe any existing structure at smaller scales and to confirm or reject all scenarios. For the AGN pair scenario, this includes high-resolution optical/infrared imaging with HST or JWST to identify the two quasars and radio interferometric observations at smaller scales to identify two compact cores with the VLBA or the next-generation Very Large Array (ngVLA; Selina et al. 2018; Nyland et al. 2018).
- It is also possible for the unresolved targets to exhibit high astrometric variability caused by the

properties of the host galaxy. If the host structure is significantly extended, as in the case of tidal features, this could contribute to the excess astrometric noise (Makarov & Secrest 2022, 2023). Despite the quality of the DECaLS imaging, due to the high redshifts of the targets, it is not possible to constrain the host galaxies with currently available optical observations from SDSS and DECaLS. Quasar host galaxy characterization will require follow-up optical/infrared imaging with higher angular resolution.

- We note that the excess astrometric noise could also be attributable to *Gaia* systematics, though this is unlikely given the careful sample selection. Future *Gaia* data releases will provide increasingly better overall astrometric measurements. Additionally, *Gaia*'s pipeline continues to develop better treatment of extended sources, and continues to increase the reliability of the astrometric excess noise parameter, increasing the number of AGN pairs identifiable in future data releases.
- An in-depth study of the overall sample illustrated that the targets sample is not particularly radio loud in comparison to a matched control sample. This likely eliminates the possibility of blazar jet activity as the main driver of the high excess astrometric noise.

Overall, we demonstrate the potential of using radio+varstrometry to systematically discover genuine kiloparsec-scale dual quasar candidates, including at redshifts greater than $z \sim 0.8$. Additionally, these results will assist in refining the targeting strategy to facilitate a more efficient identification of dual and binary AGN specifics by providing radio constraints that can be applied to a larger, more systematic search of existing radio surveys.

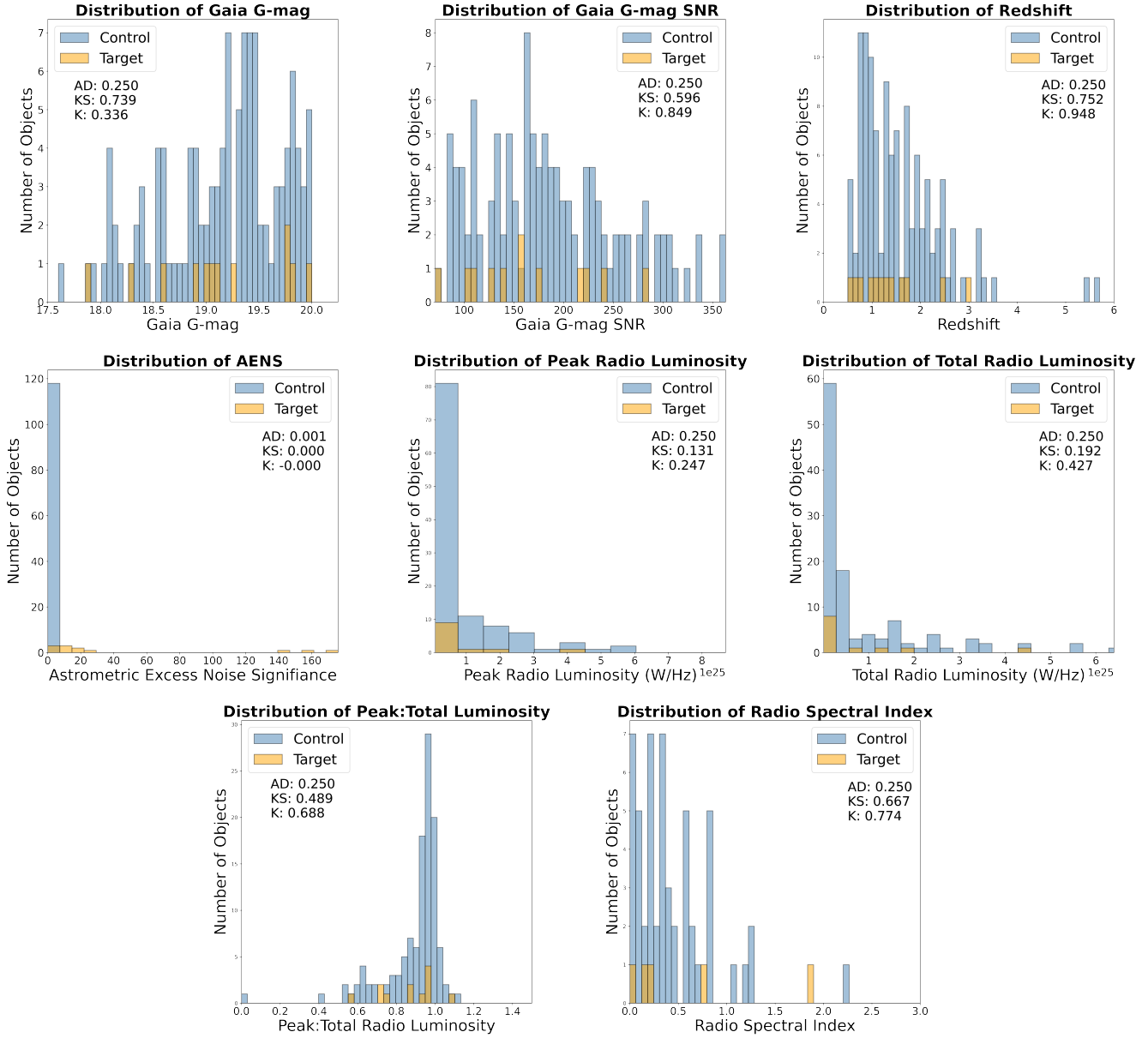


Figure 6. These histograms compare the control sample of 120 targets to a target sample of 12 targets (all with AENS > 5). The peak and total radio luminosities are those measured from VLASS. The spectral index is calculated between measurements from FIRST (at 1.4 GHz) and measurements from VLASS (at 3 GHz). The purpose of these plots is to compare the control and target samples for the important radio parameters. *Gaia* G-band magnitude, G-band magnitude SNR, and target redshift were controlled for in the creation of the control sample, and the p-values listed on the plots show the lack of disagreement between the two samples.

Facilities: *Gaia*, VLA (NRAO), Sloan, HST, VLBA

Software: astropy (Astropy Collaboration et al. (2018)), CASA (CASA Team et al. (2022)), PyBDSF (Mohan & Rafferty (2015)), TOPCAT (Taylor (2005))

1 R. W. P. gratefully acknowledges support through
 2 an appointment to the NASA Postdoctoral Program
 3 at Goddard Space Flight Center, administered by
 4 ORAU through a contract with NASA. E. S. gratefully
 5 acknowledges support from the National Radio
 6 Astronomy Observatory's Student Observing Support
 7 fellowship. This work has made use of data
 8 from the European Space Agency (ESA) mission *Gaia*
 9 (<https://www.cosmos.esa.int/gaia>), processed by the
 10 *Gaia* Data Processing and Analysis Consortium (DPAC,
 11 <https://www.cosmos.esa.int/web/gaia/dpac/consortium>).
 12 Funding for the DPAC has been provided by national
 13 institutions, in particular the institutions participating
 14 in the *Gaia* Multilateral Agreement. This research
 15 made use of Astropy, a community-developed core
 16 Python package for Astronomy (Astropy Collaboration
 17 et al. (2018)), TOPCAT (Taylor (2005)), the Common
 18 Astronomy Software Application (CASA Team et al.
 19 (2022)), and the Python Blob Detector and Source
 20 Finder (Mohan & Rafferty (2015)). Funding for the
 21 Sloan Digital Sky Survey IV has been provided by the
 22 Alfred P. Sloan Foundation, the U.S. Department of
 23 Energy Office of Science, and the Participating Institu-
 24 tions. The National Radio Astronomy Observatory is a
 25 facility of the National Science Foundation operated un-
 26 der cooperative agreement by Associated Universities,
 27 Inc. Basic research in radio astronomy at the U.S. Naval
 28 Research Laboratory is supported by 6.1 Base Funding.
 29 Construction and installation of VLITE was supported
 30 by the NRL Sustainment Restoration and Maintenance
 31 fund. This work made use of data from the VLA Low-
 32 band Ionosphere and Transient Experiment (VLITE).
 33 Construction and installation of VLITE was supported
 34 by the NRL Sustainment Restoration and Maintenance
 35 funding.

REFERENCES

- Alloin, D., Guilloreau, S., Barvainis, R., Antonucci, R., & Tacconi, L. 1997, *A&A*, 321, 24
- Astropy Collaboration, Price-Whelan, A. M., Sipőcz, B. M., et al. 2018, *AJ*, 156, 123, doi: [10.3847/1538-3881/aabc4f](https://doi.org/10.3847/1538-3881/aabc4f)
- Baars, J. W. M., Genzel, R., Pauliny-Toth, I. I. K., & Witzel, A. 1977, *A&A*, 61, 99
- Barnes, J. E., & Hernquist, L. 1992, *ARA&A*, 30, 705, doi: [10.1146/annurev.aa.30.090192.003421](https://doi.org/10.1146/annurev.aa.30.090192.003421)
- . 1996, *ApJ*, 471, 115, doi: [10.1086/177957](https://doi.org/10.1086/177957)
- Barrows, R. S., Sandberg Lacy, C. H., Kenefick, J., et al. 2013, *ApJ*, 769, 95, doi: [10.1088/0004-637X/769/2/95](https://doi.org/10.1088/0004-637X/769/2/95)
- Becker, R. H., White, R. L., & Helfand, D. J. 1995, *ApJ*, 450, 559, doi: [10.1086/176166](https://doi.org/10.1086/176166)
- Bianchi, S., Chiaberge, M., Piconcelli, E., Guainazzi, M., & Matt, G. 2008, *MNRAS*, 386, 105, doi: [10.1111/j.1365-2966.2008.13078.x](https://doi.org/10.1111/j.1365-2966.2008.13078.x)
- Bicknell, G. V., Dopita, M. A., Tsvetanov, Z. I., & Sutherland, R. S. 1998, *ApJ*, 495, 680, doi: [10.1086/305336](https://doi.org/10.1086/305336)
- Blecha, L., Snyder, G. F., Satyapal, S., & Ellison, S. L. 2018, *MNRAS*, 478, 3056, doi: [10.1093/mnras/sty1274](https://doi.org/10.1093/mnras/sty1274)
- Bolton, A. S., Schlegel, D. J., Aubourg, É., et al. 2012, *AJ*, 144, 144, doi: [10.1088/0004-6256/144/5/144](https://doi.org/10.1088/0004-6256/144/5/144)
- Brown, Vallenari, A., Prusti, T., et al. 2021, *Astronomy & Astrophysics*, 650, C3, doi: [10.1051/0004-6361/202039657e](https://doi.org/10.1051/0004-6361/202039657e)
- Burke-Spolaor, S., Blecha, L., Bogdanovic, T., et al. 2018, *The Next-Generation Very Large Array: Supermassive Black Hole Pairs and Binaries*, <https://arxiv.org/abs/1808.04368>

- Callegari, S., Mayer, L., Kazantzidis, S., et al. 2009, *The Astrophysical Journal*, 696, L89, doi: [10.1088/0004-637x/696/1/189](https://doi.org/10.1088/0004-637x/696/1/189)
- CASA Team, Bean, B., Bhatnagar, S., et al. 2022, *PASP*, 134, 114501, doi: [10.1088/1538-3873/ac9642](https://doi.org/10.1088/1538-3873/ac9642)
- Chartas, G., Eracleous, M., Agol, E., & Gallagher, S. C. 2004, *ApJ*, 606, 78, doi: [10.1086/382743](https://doi.org/10.1086/382743)
- Chen, Y., Yu, Q., & Lu, Y. 2020, *The Astrophysical Journal*, 897, 86, doi: [10.3847/1538-4357/ab9594](https://doi.org/10.3847/1538-4357/ab9594)
- Chen, Y.-C., Hwang, H.-C., Shen, Y., et al. 2022a, *ApJ*, 925, 162, doi: [10.3847/1538-4357/ac401b](https://doi.org/10.3847/1538-4357/ac401b)
- Chen, Y.-C., Liu, X., Foord, A., et al. 2022b, in *American Astronomical Society Meeting Abstracts*, Vol. 54, American Astronomical Society Meeting Abstracts, 316.08
- Ciurlo, A., Mannucci, F., Yeh, S., et al. 2023, *Astronomy & Astrophysics*, 671, L4, doi: [10.1051/0004-6361/202345853](https://doi.org/10.1051/0004-6361/202345853)
- Clarke, T., Kassim, N., Polisensky, E., et al. 2016, *arXiv e-prints*, arXiv:1603.03080, doi: [10.48550/arXiv.1603.03080](https://doi.org/10.48550/arXiv.1603.03080)
- Comerford, J. M., Griffith, R. L., Gerke, B. F., et al. 2009, *ApJL*, 702, L82, doi: [10.1088/0004-637X/702/1/L82](https://doi.org/10.1088/0004-637X/702/1/L82)
- Comerford, J. M., Pooley, D., Barrows, R. S., et al. 2015, *ApJ*, 806, 219, doi: [10.1088/0004-637X/806/2/219](https://doi.org/10.1088/0004-637X/806/2/219)
- Comerford, J. M., Schluns, K., Greene, J. E., & Cool, R. J. 2013, *ApJ*, 777, 64, doi: [10.1088/0004-637X/777/1/64](https://doi.org/10.1088/0004-637X/777/1/64)
- Condon, J. J., Cotton, W. D., Greisen, E. W., et al. 1998, *AJ*, 115, 1693, doi: [10.1086/300337](https://doi.org/10.1086/300337)
- Cornwell, T. J. 2008, *IEEE Journal of Selected Topics in Signal Processing*, 2, 793, doi: [10.1109/JSTSP.2008.2006388](https://doi.org/10.1109/JSTSP.2008.2006388)
- Cornwell, T. J., Golap, K., & Bhatnagar, S. 2005, in *Astronomical Society of the Pacific Conference Series*, Vol. 347, *Astronomical Data Analysis Software and Systems XIV*, ed. P. Shopbell, M. Britton, & R. Ebert, 86
- Dorland, B., Secrest, N., Johnson, M., et al. 2020, in *Astrometry, Earth Rotation, and Reference Systems in the GAIA era*, ed. C. Bizouard, 165–171, doi: [10.48550/arXiv.2009.02169](https://doi.org/10.48550/arXiv.2009.02169)
- Duffy, P., & Blundell, K. M. 2012, *MNRAS*, 421, 108, doi: [10.1111/j.1365-2966.2011.20239.x](https://doi.org/10.1111/j.1365-2966.2011.20239.x)
- Ellison, S. L., Patton, D. R., Mendel, J. T., & Scudder, J. M. 2011, *MNRAS*, 418, 2043, doi: [10.1111/j.1365-2966.2011.19624.x](https://doi.org/10.1111/j.1365-2966.2011.19624.x)
- Ellison, S. L., Viswanathan, A., Patton, D. R., et al. 2019, *MNRAS*, 487, 2491, doi: [10.1093/mnras/stz1431](https://doi.org/10.1093/mnras/stz1431)
- Fabircius, C., Figueras, F., Garcia-Gutierrez, A., et al. 2021, *Gaia EDR3 documentation Chapter 11: Catalogue statistics and plots*, *Gaia EDR3 documentation*, European Space Agency; *Gaia Data Processing and Analysis Consortium*, id. 11
- Ferrarese, L., & Merritt, D. 2000, *The Astrophysical Journal*, 539, L9, doi: [10.1086/312838](https://doi.org/10.1086/312838)
- Gaia Collaboration, Prusti, T., de Bruijne, J. H. J., et al. 2016, *A&A*, 595, A1, doi: [10.1051/0004-6361/201629272](https://doi.org/10.1051/0004-6361/201629272)
- Gebhardt, K., Bender, R., Bower, G., et al. 2000, *ApJL*, 539, L13, doi: [10.1086/312840](https://doi.org/10.1086/312840)
- Gil-Merino, R., Goicoechea, L. J., Shalyapin, V. N., & Oscoz, A. 2018, *A&A*, 616, A118, doi: [10.1051/0004-6361/201832737](https://doi.org/10.1051/0004-6361/201832737)
- Gordon, Y. A., Boyce, M. M., O’Dea, C. P., et al. 2021, *ApJS*, 255, 30, doi: [10.3847/1538-4365/ac05c0](https://doi.org/10.3847/1538-4365/ac05c0)
- Heckman, T. M., & Best, P. N. 2014, *ARA&A*, 52, 589, doi: [10.1146/annurev-astro-081913-035722](https://doi.org/10.1146/annurev-astro-081913-035722)
- Helmboldt, J. F., Taylor, G. B., Tremblay, S., et al. 2007, *ApJ*, 658, 203, doi: [10.1086/511005](https://doi.org/10.1086/511005)
- Hibbard, J. E., & van Gorkom, J. H. 1996, *AJ*, 111, 655, doi: [10.1086/117838](https://doi.org/10.1086/117838)
- Hopkins, P. F., Hernquist, L., Cox, T. J., & Kereš, D. 2008, *ApJS*, 175, 356, doi: [10.1086/524362](https://doi.org/10.1086/524362)
- Hopkins, P. F., & Quataert, E. 2010, *MNRAS*, 407, 1529, doi: [10.1111/j.1365-2966.2010.17064.x](https://doi.org/10.1111/j.1365-2966.2010.17064.x)
- Hwang, H.-C., Shen, Y., Zakamska, N., & Liu, X. 2020, *ApJ*, 888, 73, doi: [10.3847/1538-4357/ab5c1a](https://doi.org/10.3847/1538-4357/ab5c1a)
- Inada, N., Oguri, M., Rusu, C. E., Kayo, I., & Morokuma, T. 2014, *The Astronomical Journal*, 147, 153, doi: [10.1088/0004-6256/147/6/153](https://doi.org/10.1088/0004-6256/147/6/153)
- Inada, N., Oguri, M., Shin, M.-S., et al. 2012, *The Astronomical Journal*, 143, 119, doi: [10.1088/0004-6256/143/5/119](https://doi.org/10.1088/0004-6256/143/5/119)
- Intema, H. T., Jagannathan, P., Mooley, K. P., & Frail, D. A. 2017, *A&A*, 598, A78, doi: [10.1051/0004-6361/201628536](https://doi.org/10.1051/0004-6361/201628536)
- Jakobsson, P., Hjorth, J., Burud, I., et al. 2005, *Astronomy & Astrophysics*, 431, 103, doi: [10.1051/0004-6361:20041432](https://doi.org/10.1051/0004-6361:20041432)
- Kayser, R., Surdej, J., Condon, J. J., et al. 1990, *ApJ*, 364, 15, doi: [10.1086/169382](https://doi.org/10.1086/169382)
- Khan, F. M., Mirza, M. A., & Holley-Bockelmann, K. 2020, *MNRAS*, 492, 256, doi: [10.1093/mnras/stz3360](https://doi.org/10.1093/mnras/stz3360)
- Komossa, S., Burwitz, V., Hasinger, G., et al. 2003, *ApJL*, 582, L15, doi: [10.1086/346145](https://doi.org/10.1086/346145)
- Kormendy, J., & Richstone, D. 1995, *Nature*, 377, 131, doi: [10.1038/377131a0](https://doi.org/10.1038/377131a0)
- Koss, M., Mushotzky, R., Treister, E., et al. 2012, *ApJL*, 746, L22, doi: [10.1088/2041-8205/746/2/L22](https://doi.org/10.1088/2041-8205/746/2/L22)

- . 2011, *ApJL*, 735, L42, doi: [10.1088/2041-8205/735/2/L42](https://doi.org/10.1088/2041-8205/735/2/L42)
- Lacy, M., Myers, S. T., Chandler, C. J., & et al. 2019, VLASS Project Memo 13: Pilot and Epoch 1 Quick Look Data Release, <https://library.nrao.edu/public/memos/vla/vlass/VLASS013.pdf>
- Lemon, C., Auger, M. W., McMahan, R., et al. 2020, *MNRAS*, 494, 3491, doi: [10.1093/mnras/staa652](https://doi.org/10.1093/mnras/staa652)
- Lemon, C., Anguita, T., Auger-Williams, M. W., et al. 2023, *MNRAS*, 520, 3305, doi: [10.1093/mnras/stac3721](https://doi.org/10.1093/mnras/stac3721)
- Lemon, C. A., Auger, M. W., McMahan, R. G., & Ostrovski, F. 2018, *Monthly Notices of the Royal Astronomical Society*, 479, 5060, doi: [10.1093/mnras/sty911](https://doi.org/10.1093/mnras/sty911)
- Lindgren, L., Klioner, S. A., Hernández, J., et al. 2021, *A&A*, 649, A2, doi: [10.1051/0004-6361/202039709](https://doi.org/10.1051/0004-6361/202039709)
- Liu, X., Civano, F., Shen, Y., et al. 2013, *ApJ*, 762, 110, doi: [10.1088/0004-637X/762/2/110](https://doi.org/10.1088/0004-637X/762/2/110)
- Liu, X., Greene, J. E., Shen, Y., & Strauss, M. A. 2010a, *ApJL*, 715, L30, doi: [10.1088/2041-8205/715/1/L30](https://doi.org/10.1088/2041-8205/715/1/L30)
- Liu, X., Guo, H., Shen, Y., Greene, J. E., & Strauss, M. A. 2018, *ApJ*, 862, 29, doi: [10.3847/1538-4357/aac9cb](https://doi.org/10.3847/1538-4357/aac9cb)
- Liu, X., Shen, Y., & Strauss, M. A. 2011, *ApJL*, 736, L7, doi: [10.1088/2041-8205/736/1/L7](https://doi.org/10.1088/2041-8205/736/1/L7)
- Liu, X., Shen, Y., Strauss, M. A., & Greene, J. E. 2010b, *ApJ*, 708, 427, doi: [10.1088/0004-637X/708/1/427](https://doi.org/10.1088/0004-637X/708/1/427)
- Lyke, B. W., Higley, A. N., McLane, J. N., et al. 2020, *ApJS*, 250, 8, doi: [10.3847/1538-4365/aba623](https://doi.org/10.3847/1538-4365/aba623)
- Lyu, Y., & Liu, X. 2016, *MNRAS*, 463, 24, doi: [10.1093/mnras/stw1945](https://doi.org/10.1093/mnras/stw1945)
- MacLeod, C. L., Ivezić, Ž., Kochanek, C. S., et al. 2010, *ApJ*, 721, 1014, doi: [10.1088/0004-637X/721/2/1014](https://doi.org/10.1088/0004-637X/721/2/1014)
- MacLeod, C. L., Ivezić, Ž., Sesar, B., et al. 2012, *The Astrophysical Journal*, 753, 106, doi: [10.1088/0004-637x/753/2/106](https://doi.org/10.1088/0004-637x/753/2/106)
- Madau, P., & Dickinson, M. 2014, *ARA&A*, 52, 415, doi: [10.1146/annurev-astro-081811-125615](https://doi.org/10.1146/annurev-astro-081811-125615)
- Makarov, V., Berghea, C., Boboltz, D., et al. 2012, *Quasometry, Its Use and Purpose*, <https://arxiv.org/abs/1202.5283>
- Makarov, V. V., Berghea, C. T., Frouard, J., Fey, A., & Schmitt, H. R. 2019, *The Astrophysical Journal*, 873, 132, doi: [10.3847/1538-4357/aafalc](https://doi.org/10.3847/1538-4357/aafalc)
- Makarov, V. V., Frouard, J., Berghea, C. T., et al. 2017, *The Astrophysical Journal*, 835, L30, doi: [10.3847/2041-8213/835/2/L30](https://doi.org/10.3847/2041-8213/835/2/L30)
- Makarov, V. V., & Goldin, A. 2016, *ApJS*, 224, 19, doi: [10.3847/0067-0049/224/2/19](https://doi.org/10.3847/0067-0049/224/2/19)
- Makarov, V. V., & Secrest, N. J. 2022, *ApJ*, 933, 28, doi: [10.3847/1538-4357/ac7047](https://doi.org/10.3847/1538-4357/ac7047)
- . 2023, *ApJS*, 264, 4, doi: [10.3847/1538-4365/ac97f0](https://doi.org/10.3847/1538-4365/ac97f0)
- Mannucci, F., Pancino, E., Belfiore, F., et al. 2022, *Nature Astronomy*, 6, 1185, doi: [10.1038/s41550-022-01761-5](https://doi.org/10.1038/s41550-022-01761-5)
- McConnell, D., Hale, C. L., Lenc, E., et al. 2020, *PASA*, 37, e048, doi: [10.1017/pasa.2020.41](https://doi.org/10.1017/pasa.2020.41)
- Merritt, D. 2013, *Dynamics and Evolution of Galactic Nuclei* (American Astronomical Society)
- Mihos, J. C., & Hernquist, L. 1996, *ApJ*, 464, 641, doi: [10.1086/177353](https://doi.org/10.1086/177353)
- Mohan, N., & Rafferty, D. 2015, *PyBDSF: Python Blob Detection and Source Finder*, *Astrophysics Source Code Library*, record ascl:1502.007. <http://ascl.net/1502.007>
- Morgan, W. W., Keenan, P. C., & Kellman, E. 1943, *An atlas of stellar spectra, with an outline of spectral classification* (American Astronomical Society)
- Nyland, K., Mukherjee, D., Lacy, M., et al. 2018, *Science with an ngVLA: Radio Jet-ISM Feedback on Sub-galactic Scales*. <https://arxiv.org/abs/1810.07526>
- Nyland, K., Dong, D. Z., Patil, P., et al. 2020, *ApJ*, 905, 74, doi: [10.3847/1538-4357/abc341](https://doi.org/10.3847/1538-4357/abc341)
- O’Dea, C. P. 1998, *PASP*, 110, 493, doi: [10.1086/316162](https://doi.org/10.1086/316162)
- O’Dea, C. P., & Saikia, D. J. 2021, *A&A Rv*, 29, 3, doi: [10.1007/s00159-021-00131-w](https://doi.org/10.1007/s00159-021-00131-w)
- O’Dowd, M. J., Bate, N. F., Webster, R. L., Labrie, K., & Rogers, J. 2015, *The Astrophysical Journal*, 813, 62, doi: [10.1088/0004-637x/813/1/62](https://doi.org/10.1088/0004-637x/813/1/62)
- Orienti, M., & Dallacasa, D. 2014, *MNRAS*, 438, 463, doi: [10.1093/mnras/stt2217](https://doi.org/10.1093/mnras/stt2217)
- Osterbrock, D. E. 1989, *Astrophysics of gaseous nebulae and active galactic nuclei* (University Science Books)
- . 1993, *RMxAA*, 26, 65
- Owen, F. N., O’Dea, C. P., Inoue, M., & Eilek, J. A. 1985, *ApJL*, 294, L85, doi: [10.1086/184514](https://doi.org/10.1086/184514)
- Patil, P., Whittle, M., Nyland, K., et al. 2021, *Astronomische Nachrichten*, 342, 1166, doi: [10.1002/asna.20210078](https://doi.org/10.1002/asna.20210078)
- . 2022, *ApJ*, 934, 26, doi: [10.3847/1538-4357/ac71b0](https://doi.org/10.3847/1538-4357/ac71b0)
- Perley, R. A., & Butler, B. J. 2017, *ApJS*, 230, 7, doi: [10.3847/1538-4365/aa6df9](https://doi.org/10.3847/1538-4365/aa6df9)
- Pfeifle, R. 2023
- Pfeifle, R. W., Rothberg, B., Weaver, K. A., et al. 2023, *ApJ*, 945, 167, doi: [10.3847/1538-4357/acbd45](https://doi.org/10.3847/1538-4357/acbd45)
- Pfeifle, R. W., Satyapal, S., Manzano-King, C., et al. 2019a, *ApJ*, 883, 167, doi: [10.3847/1538-4357/ab3a9b](https://doi.org/10.3847/1538-4357/ab3a9b)
- Pfeifle, R. W., Satyapal, S., Secrest, N. J., et al. 2019b, *ApJ*, 875, 117, doi: [10.3847/1538-4357/ab07bc](https://doi.org/10.3847/1538-4357/ab07bc)
- Piconcelli, E., Vignali, C., Bianchi, S., et al. 2010, *ApJL*, 722, L147, doi: [10.1088/2041-8205/722/2/L147](https://doi.org/10.1088/2041-8205/722/2/L147)
- Planck Collaboration, Aghanim, N., Akrami, Y., et al. 2020, *A&A*, 641, A6, doi: [10.1051/0004-6361/201833910](https://doi.org/10.1051/0004-6361/201833910)

- Polisensky, E., Lane, W. M., Hyman, S. D., et al. 2016, *ApJ*, 832, 60, doi: [10.3847/0004-637X/832/1/60](https://doi.org/10.3847/0004-637X/832/1/60)
- Rau, U., & Cornwell, T. J. 2011, *A&A*, 532, A71, doi: [10.1051/0004-6361/201117104](https://doi.org/10.1051/0004-6361/201117104)
- Richards, G. T., Strauss, M. A., Fan, X., et al. 2006, *AJ*, 131, 2766, doi: [10.1086/503559](https://doi.org/10.1086/503559)
- Rodriguez, C., Taylor, G. B., Zavala, R. T., et al. 2006, *ApJ*, 646, 49, doi: [10.1086/504825](https://doi.org/10.1086/504825)
- Rusu, C. E., Berghea, C. T., Fassnacht, C. D., et al. 2019, *Monthly Notices of the Royal Astronomical Society*, 486, 4987, doi: [10.1093/mnras/stz1142](https://doi.org/10.1093/mnras/stz1142)
- Satyapal, S., Secrest, N. J., Ricci, C., et al. 2017, *ApJ*, 848, 126, doi: [10.3847/1538-4357/aa88ca](https://doi.org/10.3847/1538-4357/aa88ca)
- Schechter, P. L., Gregg, M. D., Becker, R. H., Helfand, D. J., & White, R. L. 1998, *The Astronomical Journal*, 115, 1371, doi: [10.1086/300294](https://doi.org/10.1086/300294)
- Schweizer, F. 1982, *ApJ*, 252, 455, doi: [10.1086/159573](https://doi.org/10.1086/159573)
- . 1996, *AJ*, 111, 109, doi: [10.1086/117765](https://doi.org/10.1086/117765)
- Selina, R. J., Murphy, E. J., McKinnon, M., et al. 2018, in *Astronomical Society of the Pacific Conference Series*, Vol. 517, *Science with a Next Generation Very Large Array*, ed. E. Murphy, 15, doi: [10.48550/arXiv.1810.08197](https://doi.org/10.48550/arXiv.1810.08197)
- Sesar, B., Stuart, J. S., Ivezić, Ž., et al. 2011, *AJ*, 142, 190, doi: [10.1088/0004-6256/142/6/190](https://doi.org/10.1088/0004-6256/142/6/190)
- Sexton, R. O., Matzko, W., Darden, N., Canalizo, G., & Gorjian, V. 2021, *MNRAS*, 500, 2871, doi: [10.1093/mnras/staa3278](https://doi.org/10.1093/mnras/staa3278)
- Shen, Y. 2021, *Nature Astronomy*, 5, 787, doi: [10.1038/s41550-021-01385-6](https://doi.org/10.1038/s41550-021-01385-6)
- Shimwell, T. W., Tasse, C., Hardcastle, M. J., et al. 2019, *A&A*, 622, A1, doi: [10.1051/0004-6361/201833559](https://doi.org/10.1051/0004-6361/201833559)
- Shimwell, T. W., Hardcastle, M. J., Tasse, C., et al. 2022, *A&A*, 659, A1, doi: [10.1051/0004-6361/202142484](https://doi.org/10.1051/0004-6361/202142484)
- Sluse, D., Chantry, V., Magain, P., Courbin, F., & Meylan, G. 2012, *Astronomy & Astrophysics*, 538, A99, doi: [10.1051/0004-6361/201015844](https://doi.org/10.1051/0004-6361/201015844)
- Smith, K. L., Shields, G. A., Bonning, E. W., et al. 2010, *ApJ*, 716, 866, doi: [10.1088/0004-637X/716/1/866](https://doi.org/10.1088/0004-637X/716/1/866)
- Somerville, R. S., & Davé, R. 2015, *Annual Review of Astronomy and Astrophysics*, 53, 51, doi: [10.1146/annurev-astro-082812-140951](https://doi.org/10.1146/annurev-astro-082812-140951)
- Souchay, J., Secrest, N., Lambert, S., et al. 2022, *A&A*, 660, A16, doi: [10.1051/0004-6361/202141915](https://doi.org/10.1051/0004-6361/202141915)
- Taylor, M. B. 2005, in *Astronomical Society of the Pacific Conference Series*, Vol. 347, *Astronomical Data Analysis Software and Systems XIV*, ed. P. Shopbell, M. Britton, & R. Ebert, 29
- Toomre, A., & Toomre, J. 1972, *ApJ*, 178, 623, doi: [10.1086/151823](https://doi.org/10.1086/151823)
- Tremmel, M., Governato, F., Volonteri, M., Quinn, T. R., & Pontzen, A. 2018, *MNRAS*, 475, 4967, doi: [10.1093/mnras/sty139](https://doi.org/10.1093/mnras/sty139)
- U, V., Medling, A., Sanders, D., et al. 2013, *ApJ*, 775, 115, doi: [10.1088/0004-637X/775/2/115](https://doi.org/10.1088/0004-637X/775/2/115)
- Volonteri, M., Dubois, Y., Pichon, C., & Devriendt, J. 2016, *MNRAS*, 460, 2979, doi: [10.1093/mnras/stw1123](https://doi.org/10.1093/mnras/stw1123)
- Wang, H.-C., Wang, J.-X., Gu, M.-F., & Liao, M. 2023, *Monthly Notices of the Royal Astronomical Society: Letters*, doi: [10.1093/mnrasl/slad069](https://doi.org/10.1093/mnrasl/slad069)
- Wang, J.-M., Chen, Y.-M., Hu, C., et al. 2009, *ApJL*, 705, L76, doi: [10.1088/0004-637X/705/1/L76](https://doi.org/10.1088/0004-637X/705/1/L76)
- Wang, L., Greene, J. E., Ju, W., et al. 2017, *ApJ*, 834, 129, doi: [10.3847/1538-4357/834/2/129](https://doi.org/10.3847/1538-4357/834/2/129)
- Xu, D., & Komossa, S. 2009, *ApJL*, 705, L20, doi: [10.1088/0004-637X/705/1/L20](https://doi.org/10.1088/0004-637X/705/1/L20)
- Yu, Q. 2002, *MNRAS*, 331, 935, doi: [10.1046/j.1365-8711.2002.05242.x](https://doi.org/10.1046/j.1365-8711.2002.05242.x)
- Zhang, L., Zhang, Z.-Y., Nightingale, J. W., et al. 2022, *arXiv e-prints*, arXiv:2212.07027, doi: [10.48550/arXiv.2212.07027](https://doi.org/10.48550/arXiv.2212.07027)

9. APPENDIX A: INDIVIDUAL TARGET VLA OBSERVATIONS

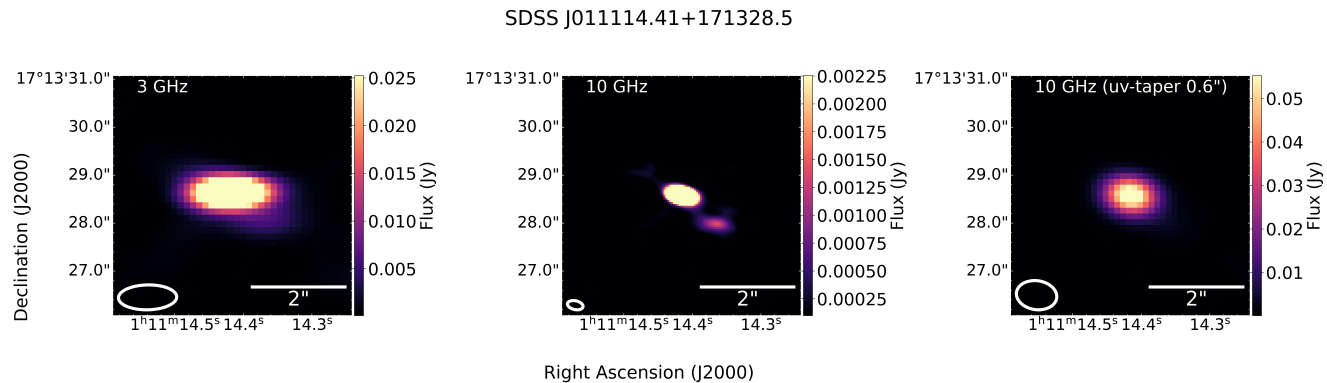


Figure 1. SDSSJ011114.41+171328.5: Left: VLA 3 GHz observations with a $1.22'' \times 0.52''$ beam. Middle: VLA 10 GHz observations with a $0.27'' \times 0.21''$ beam. Right: VLA 10 GHz uv-tapered observations with a $0.84'' \times 0.60''$ beam. Scale is 8.26 kiloparsecs per arcsecond.

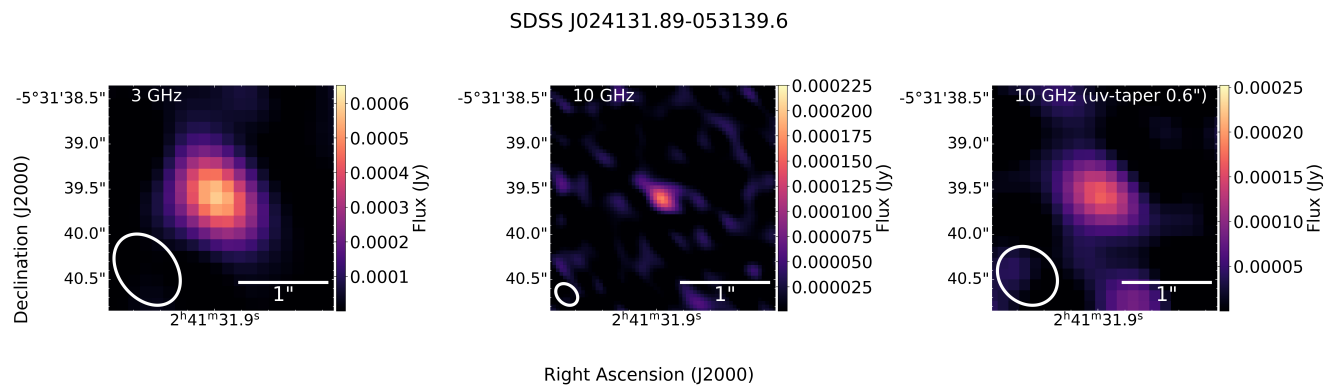


Figure 2. SDSSJ024131.89-053139.6: Left: VLA 3 GHz observations with a $0.87'' \times 0.63''$ beam. Middle: VLA 10 GHz observations with a $0.19'' \times 0.17''$ beam. Right: VLA 10 GHz uv-tapered observations with a $0.71'' \times 0.60''$ beam. Scale is 7.50 kiloparsecs per arcsecond.

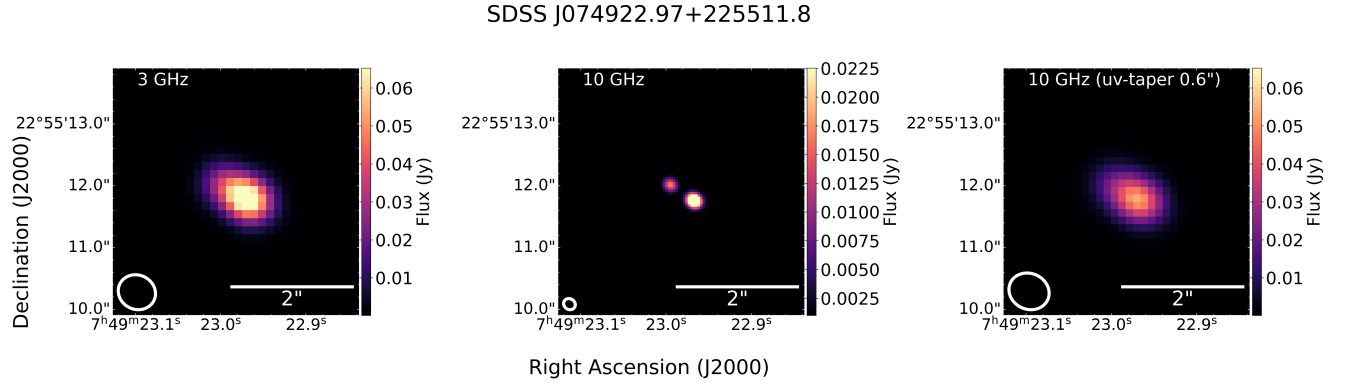


Figure 3. SDSSJ074922.97+225511.8: Left: VLA 3 GHz observations with a $0.62'' \times 0.55''$ beam. Middle: VLA 10 GHz observations with a $0.24'' \times 0.17''$ beam. Right: VLA 10 GHz uv-tapered observations with a $0.66'' \times 0.57''$ beam. Scale is 8.32 kiloparsecs per arcsecond.

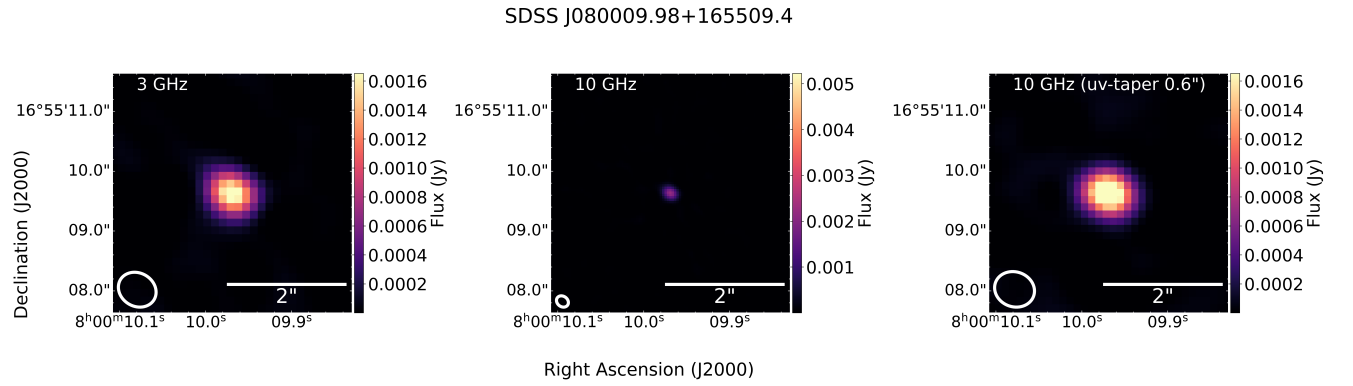


Figure 4. SDSSJ080009.98+165509.4: Left: VLA 3 GHz observations with a $0.65'' \times 0.55''$ beam. Middle: VLA 10 GHz observations with a $0.23'' \times 0.17''$ beam. Right: VLA 10 GHz uv-tapered observations with a $0.67'' \times 0.58''$ beam. Scale is 7.14 kiloparsecs per arcsecond.

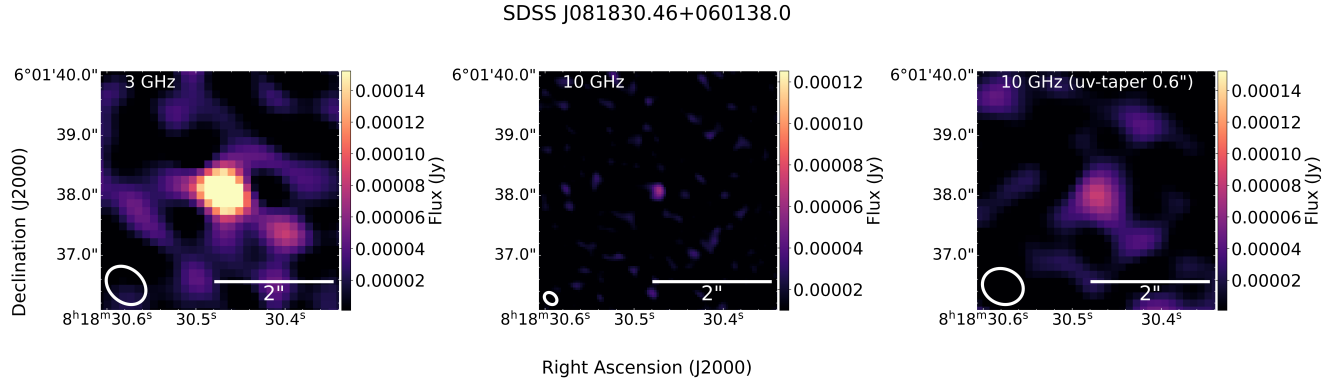


Figure 5. SDSSJ081830.46+060138.0: Left: VLA 3 GHz observations with a $0.73'' \times 0.56''$ beam. Middle: VLA 10 GHz observations with a $0.21'' \times 0.18''$ beam. Right: VLA 10 GHz uv-tapered observations with a $0.69'' \times 0.58''$ beam. Scale is 8.20 kiloparsecs per arcsecond.

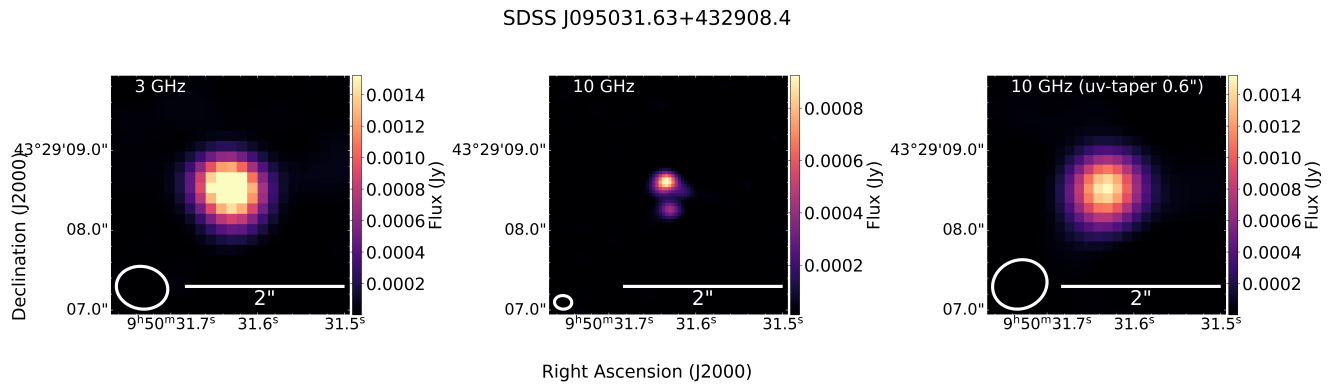


Figure 6. SDSSJ095031.63+432908.4: Left: VLA 3 GHz observations with a $0.65'' \times 0.53''$ beam. Middle: VLA 10 GHz observations with a $0.21'' \times 0.17''$ beam. Right: VLA 10 GHz uv-tapered observations with a $0.69'' \times 0.61''$ beam. Scale is 8.46 kiloparsecs per arcsecond.

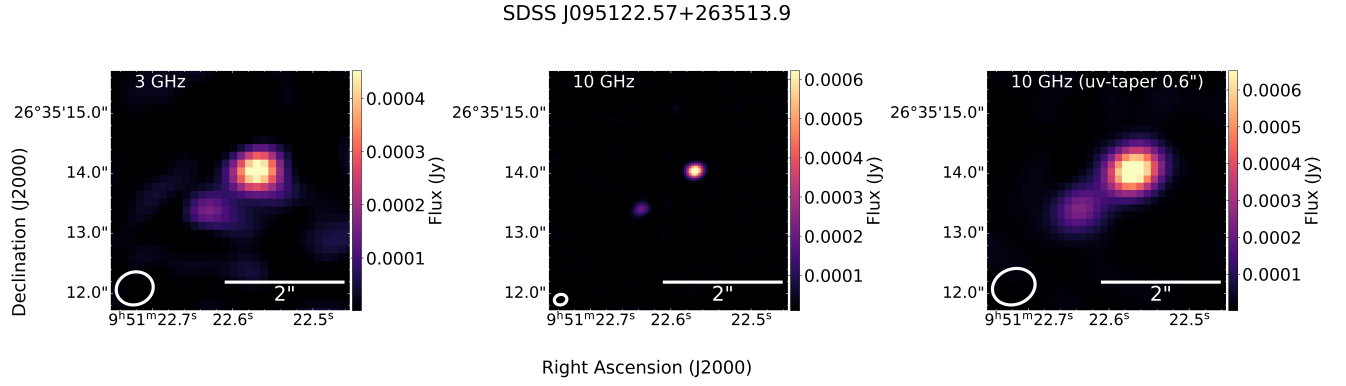


Figure 7. SDSSJ095122.57+263513.9: Left: VLA 3 GHz observations with a $0.62'' \times 0.54''$ beam. Middle: VLA 10 GHz observations with a $0.21'' \times 0.17''$ beam. Right: VLA 10 GHz uv-tapered observations with a $0.72'' \times 0.59''$ beam. Scale is 8.23 kiloparsecs per arcsecond.

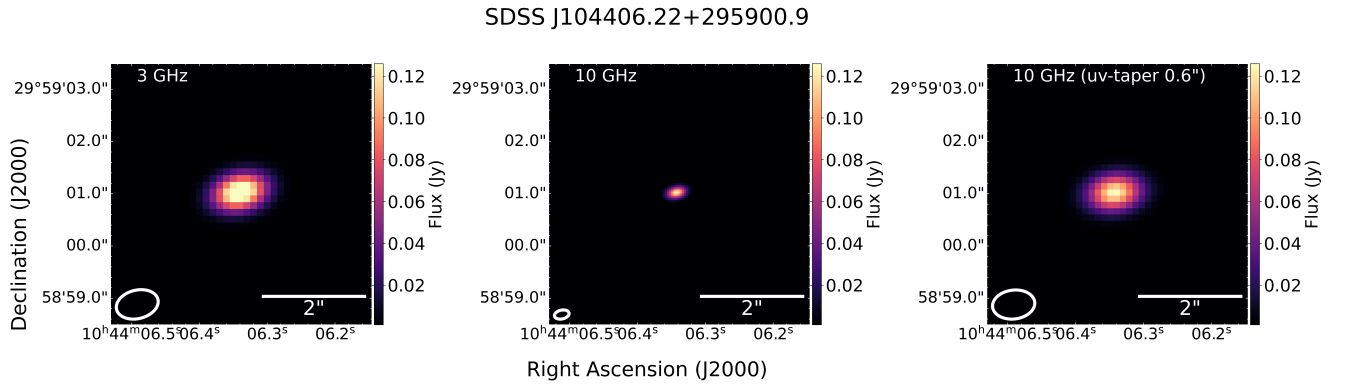


Figure 8. SDSSJ104406.33+295900.9: Left: VLA 3 GHz observations with a $0.82'' \times 0.54''$ beam. Middle: VLA 10 GHz observations with a $0.18'' \times 0.15''$ beam. Right: VLA 10 GHz uv-tapered observations with a $0.81'' \times 0.55''$ beam. Scale is 7.77 kiloparsecs per arcsecond.

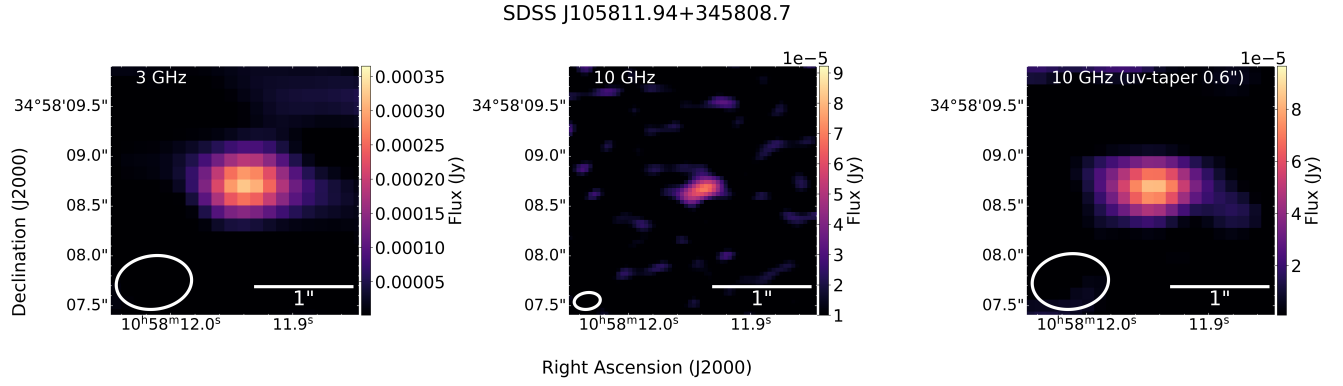


Figure 9. SDSSJ105811.94+240217.4: Left: VLA 3 GHz observations with a $0.76'' \times 0.54''$ beam. Middle: VLA 10 GHz observations with a $0.12'' \times 0.16''$ beam. Right: VLA 10 GHz uv-tapered observations with a $0.76'' \times 0.55''$ beam. Scale is 8.17 kiloparsecs per arcsecond.

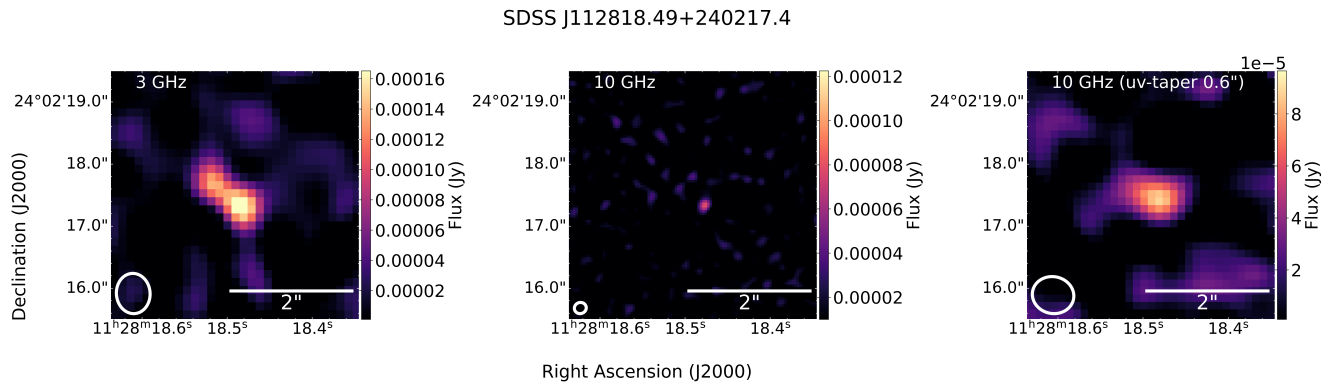


Figure 10. SDSSJ112818.49+240217.4: Left: VLA 3 GHz observations with a $0.65'' \times 0.54''$ beam. Middle: VLA 10 GHz observations with a $0.25'' \times 0.17''$ beam. Right: VLA 10 GHz uv-tapered observations with a $0.67'' \times 0.59''$ beam. Scale is 8.47 kiloparsecs per arcsecond.

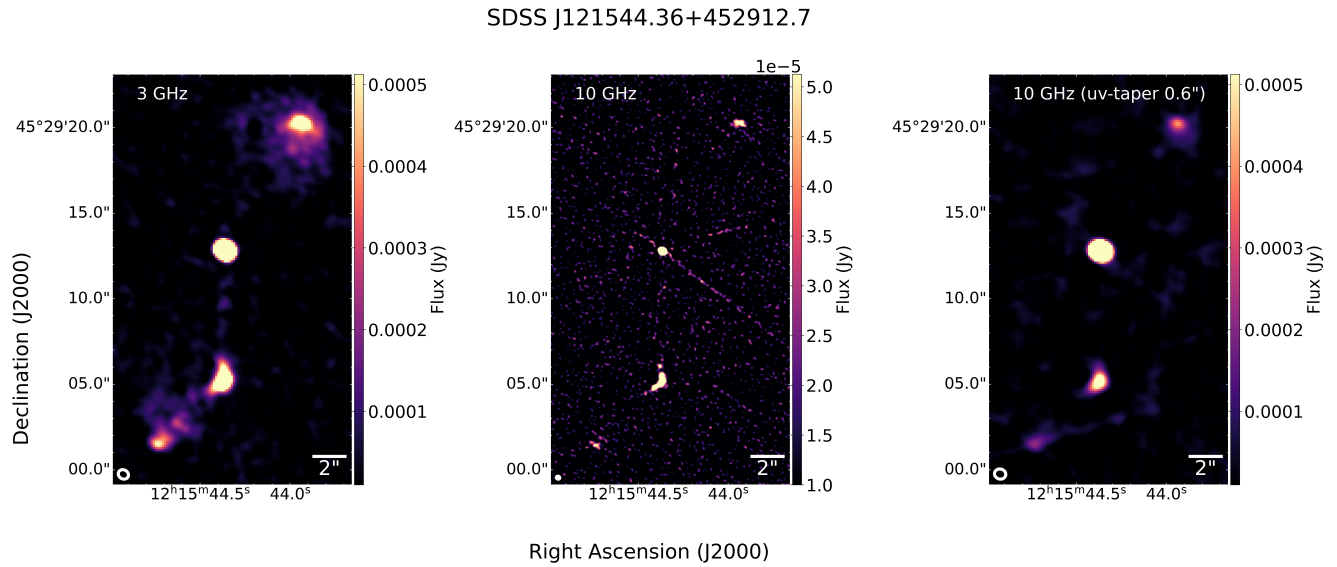


Figure 11. SDSSJ121544.36+452912.7: Left: VLA 3 GHz observations with a $0.62'' \times 0.53''$ beam. Middle: VLA 10 GHz observations with a $0.23'' \times 0.16''$ beam. Right: VLA 10 GHz uv-tapered observations with a $0.66'' \times 0.58''$ beam. Scale is 8.17 kiloparsecs per arcsecond.

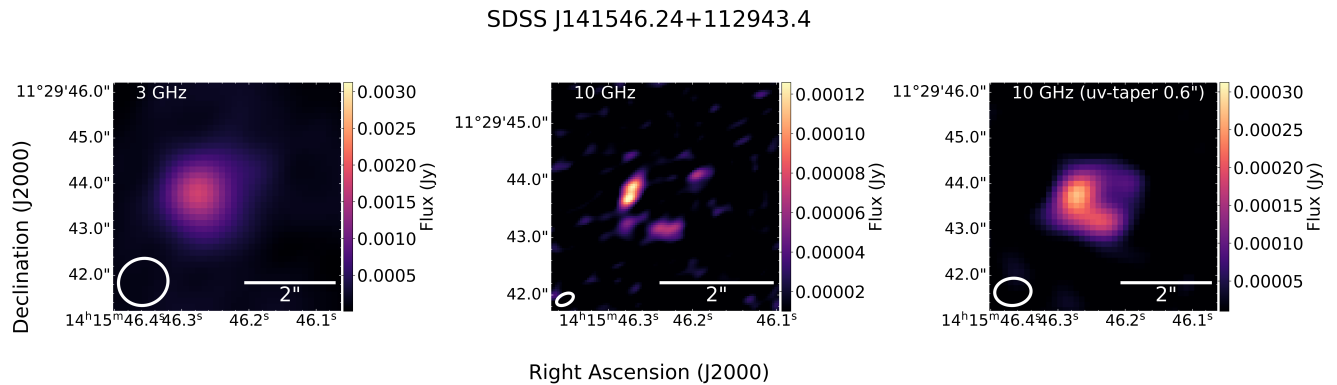


Figure 12. SDSSJ141546.24+112943.4: Left: VLA 3 GHz observations with a $1.09'' \times 1.02''$ beam. Middle: VLA 10 GHz observations with a $0.19'' \times 0.16''$ beam. Right: VLA 10 GHz uv-tapered observations with a $0.79'' \times 0.59''$ beam. Scale is 8.07 kiloparsecs per arcsecond.

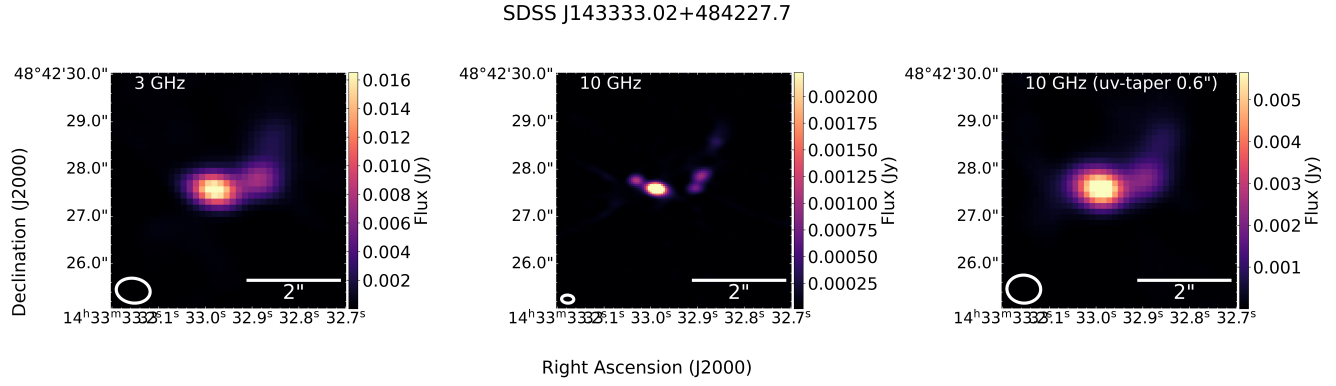


Figure 13. SDSSJ143333.02+484227.7: Left: VLA 3 GHz observations with a $0.72'' \times 0.52''$ beam. Middle: VLA 10 GHz observations with a $0.21'' \times 0.17''$ beam. Right: VLA 10 GHz uv-tapered observations with a $0.71'' \times 0.59''$ beam. Scale is 8.37 kiloparsecs per arcsecond.

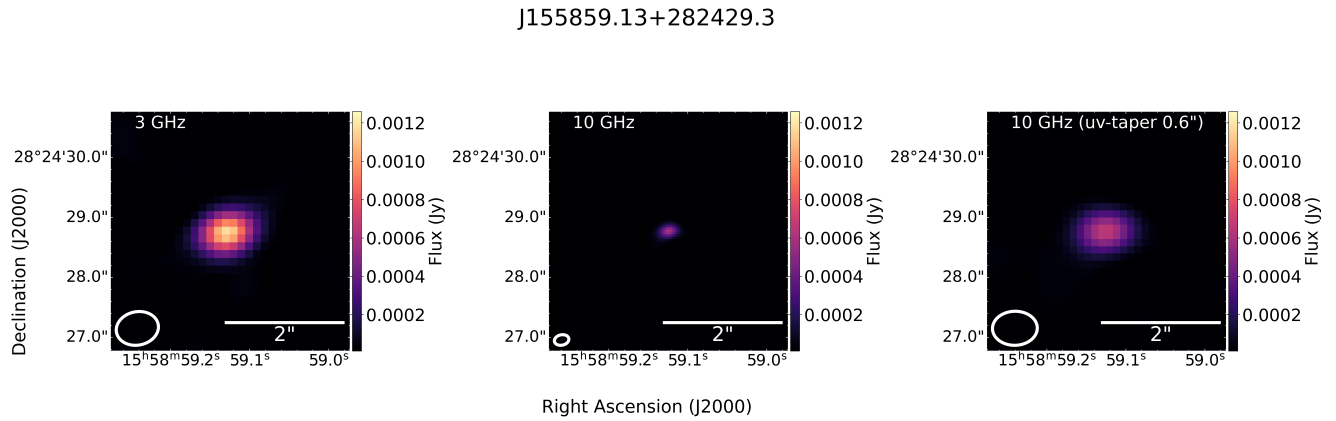


Figure 14. SDSSJ155859.13+282429.3: Left: VLA 3 GHz observations with a $0.71'' \times 0.56''$ beam. Middle: VLA 10 GHz observations with a $0.31'' \times 0.18''$ beam. Right: VLA 10 GHz uv-tapered observations with a $0.74'' \times 0.56''$ beam. Scale is 8.21 kiloparsecs per arcsecond.

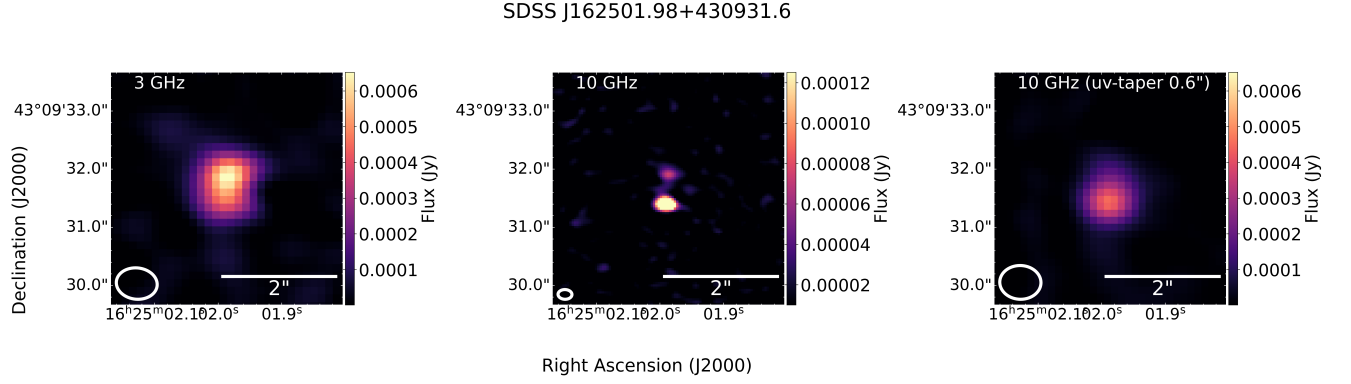


Figure 15. SDSSJ162501.98+430931.6: Left: VLA 3 GHz observations with a $0.71'' \times 0.54''$ beam. Middle: VLA 10 GHz observations with a $0.33'' \times 0.18''$ beam. Right: VLA 10 GHz uv-tapered observations with a $0.71'' \times 0.58''$ beam. Scale is 8.47 kiloparsecs per arcsecond.

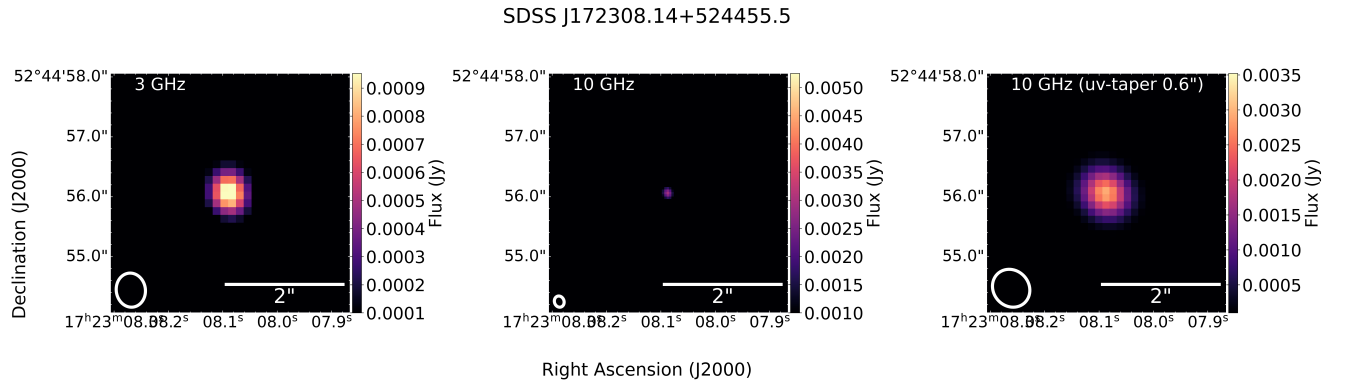


Figure 16. SDSSJ172308.14+524455.5: Left: VLA 3 GHz observations with a $0.57'' \times 0.49''$ beam. Middle: VLA 10 GHz observations with a $0.28'' \times 0.16''$ beam. Right: VLA 10 GHz uv-tapered observations with a $0.66'' \times 0.59''$ beam. Scale is 8.44 kiloparsecs per arcsecond.

SDSS J173330.80+552030.9

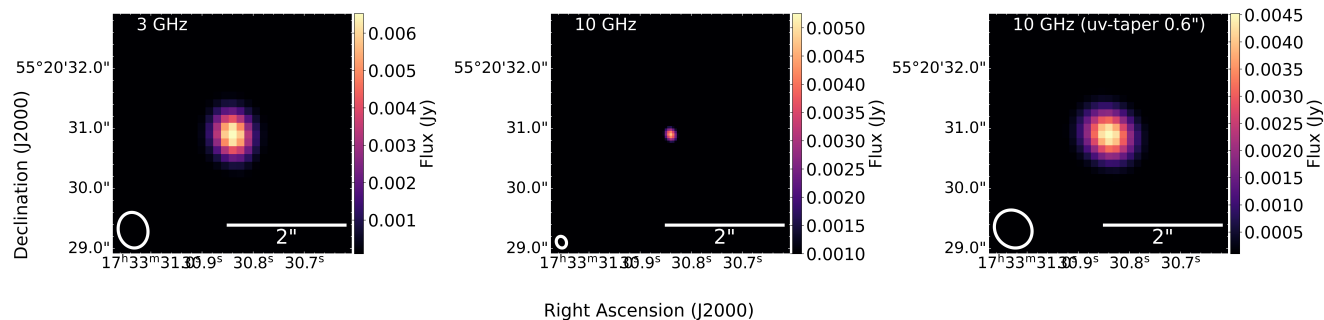


Figure 17. SDSSJ173330.80+552030.9: Left: VLA 3 GHz observations with a $0.59'' \times 0.49''$ beam. Middle: VLA 10 GHz observations with a $0.19'' \times 0.17''$ beam. Right: VLA 10 GHz uv-tapered observations with a $0.66'' \times 0.59''$ beam. Scale is 8.29 kiloparsecs per arcsecond.

SDSS J210947.09+065634.7

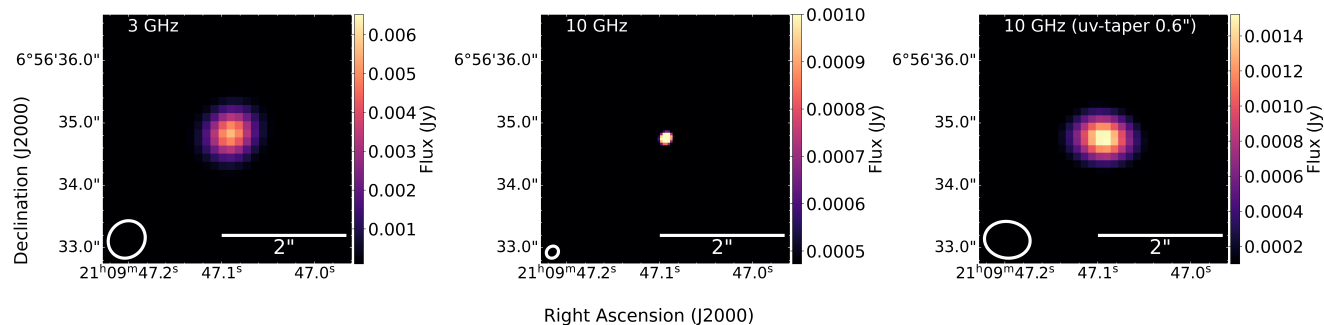
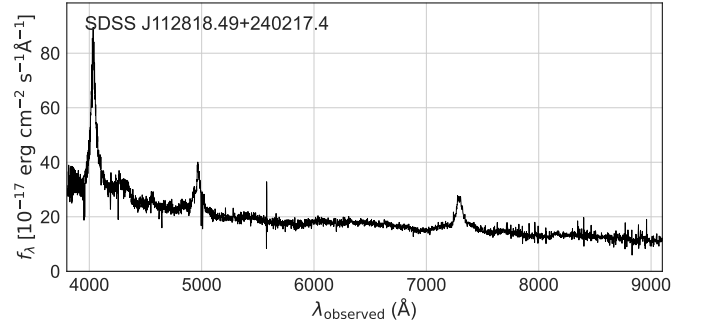
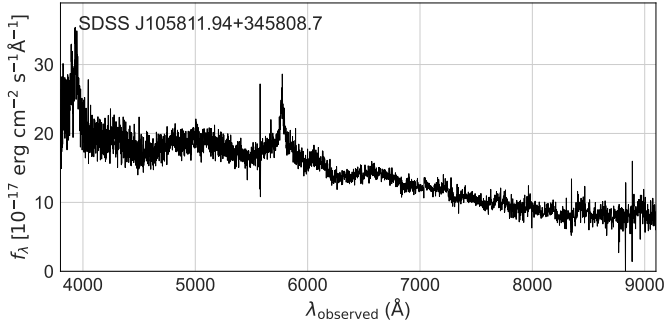
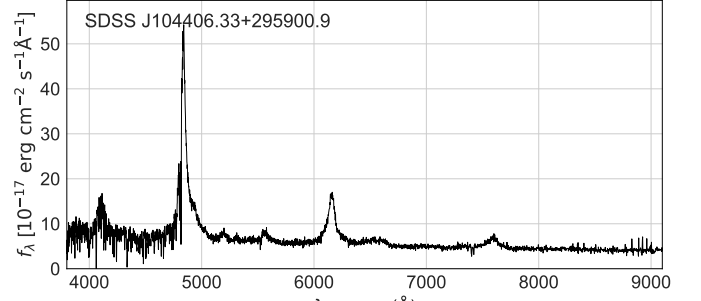
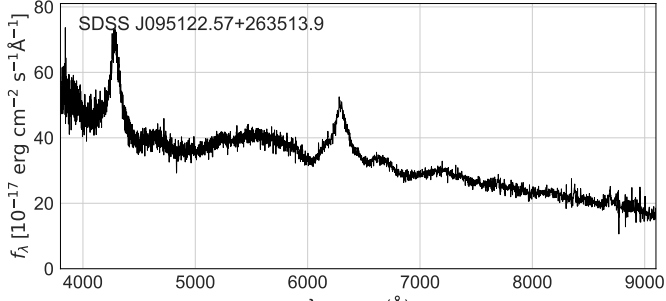
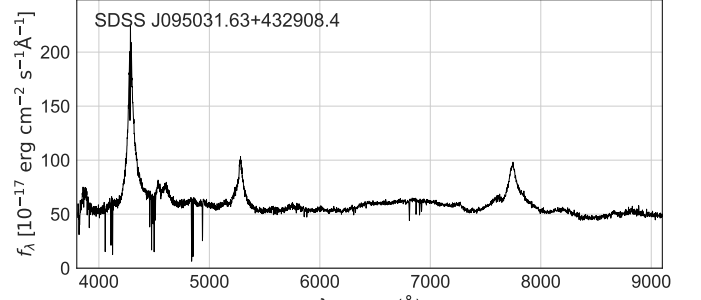
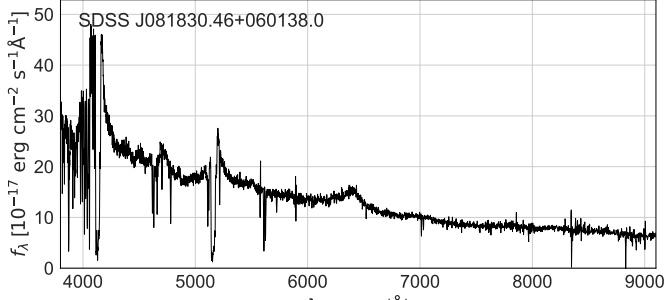
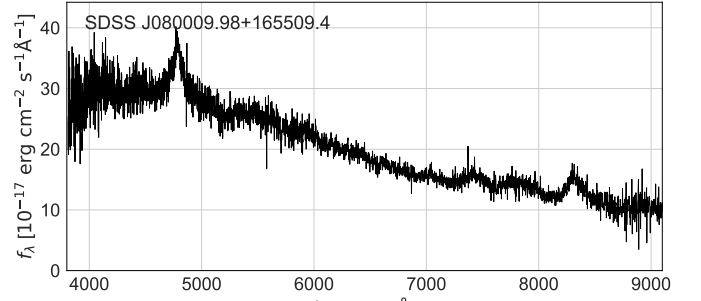
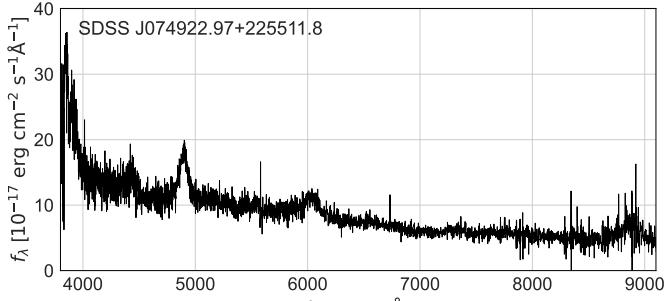
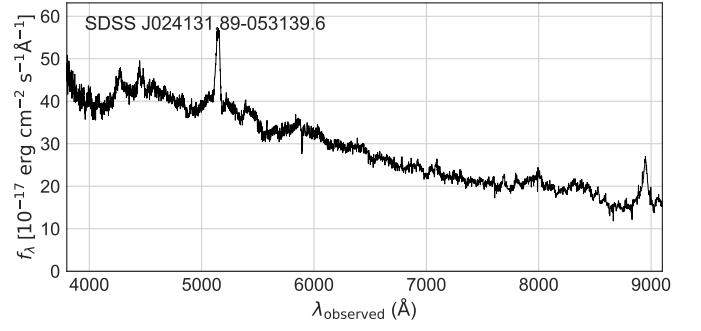
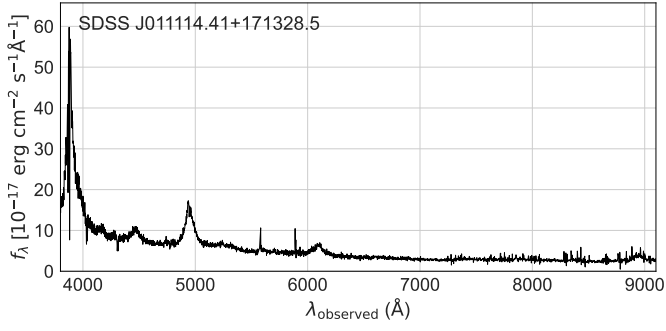


Figure 18. SDSSJ210947.09+065634.7: Left: VLA 3 GHz observations with a $0.63'' \times 0.57''$ beam. Middle: VLA 10 GHz observations with a $0.26'' \times 0.16''$ beam. Right: VLA 10 GHz uv-tapered observations with a $0.73'' \times 0.58''$ beam. Scale is 7.77 kiloparsecs per arcsecond.

10. APPENDIX B: INDIVIDUAL TARGET OPTICAL SPECTRA



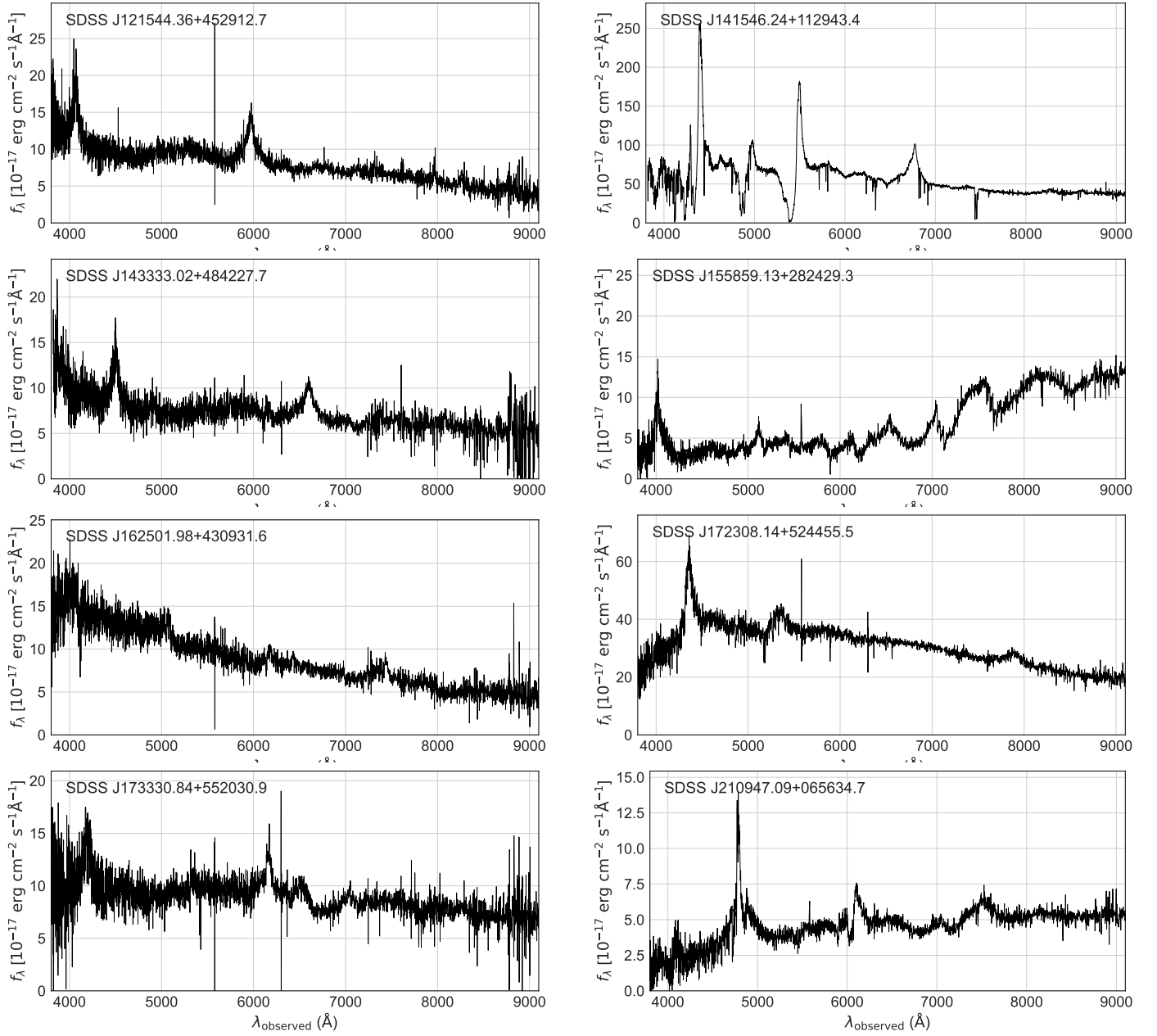
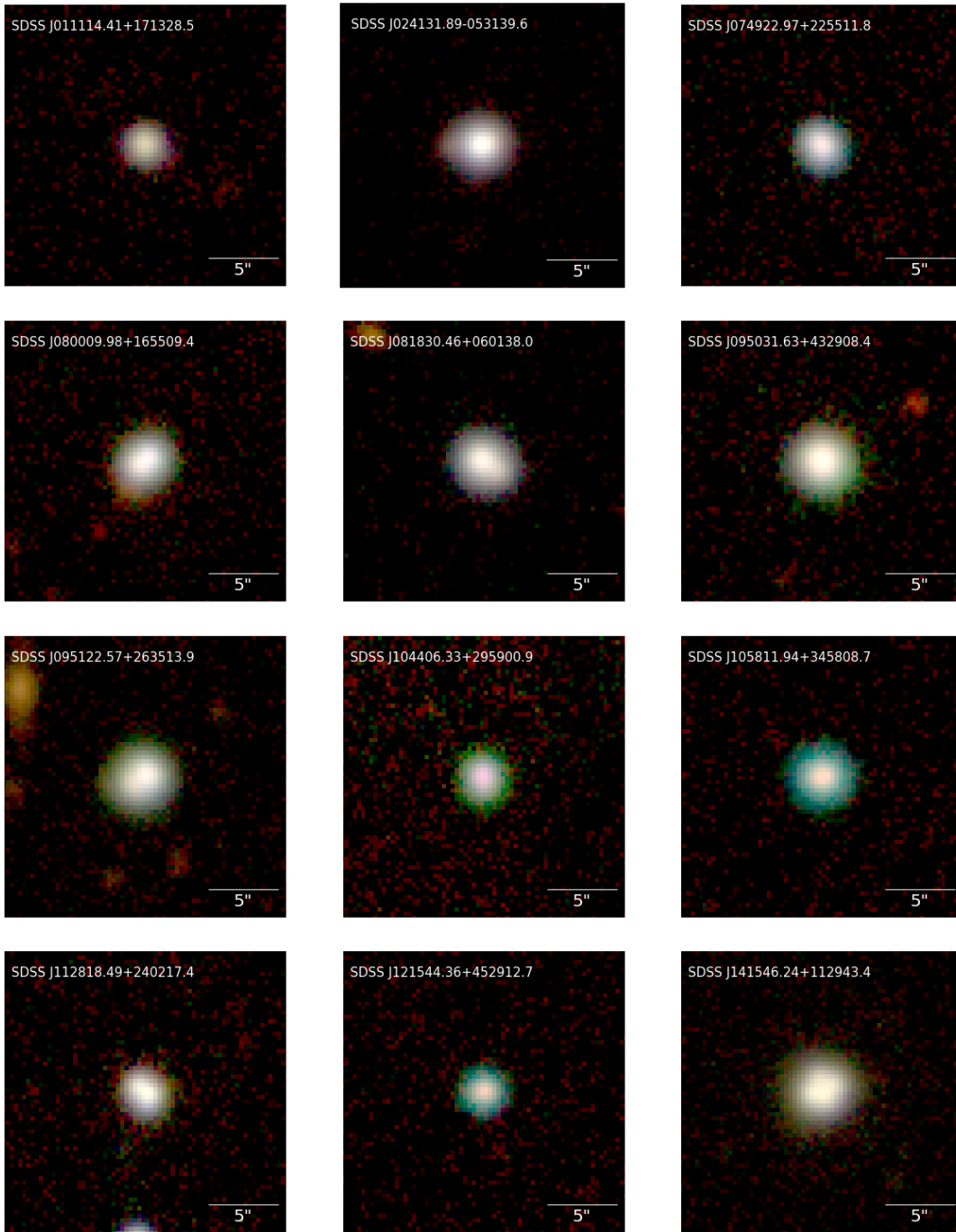


Figure 19. Observed SDSS spectra for the entire sample of 18 targets. These panels display the observed SDSS spectrum ($\sim 4000\text{\AA}$ to $\sim 9000\text{\AA}$) available for each system in the sample; these spectra are not redshift corrected. The designation for each system is listed in the top left corner of each panel. As noted in Section 7.1, four of these systems likely comprise a foreground star and background quasar caught in projection (J0241-0531, J1558+2824, J1723+5244, J2109+0656).

11. APPENDIX C: INDIVIDUAL TARGET OPTICAL IMAGING



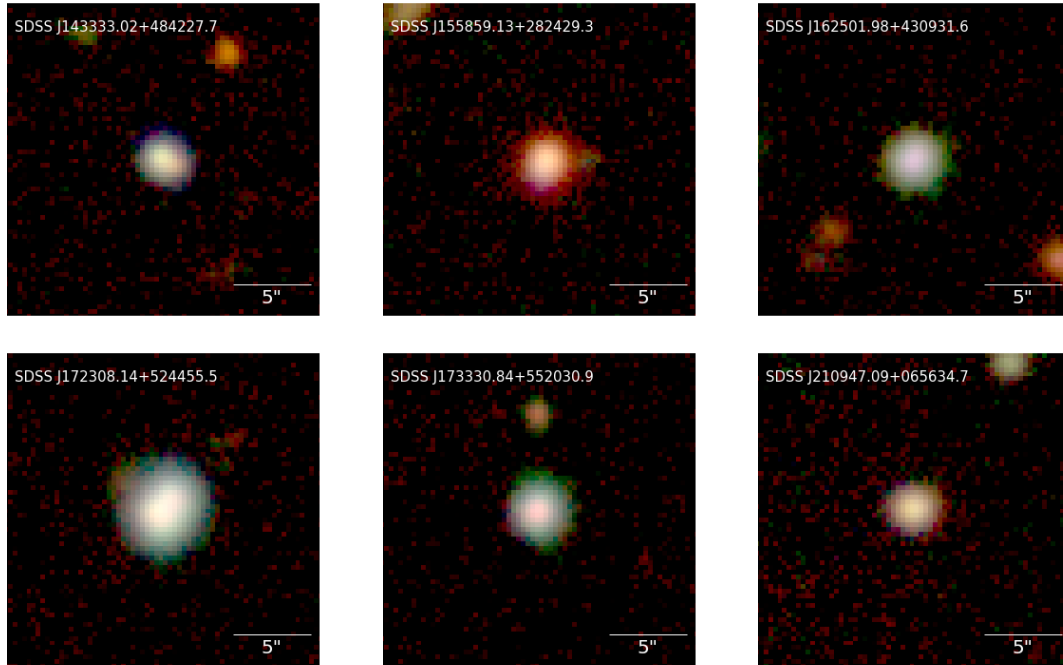
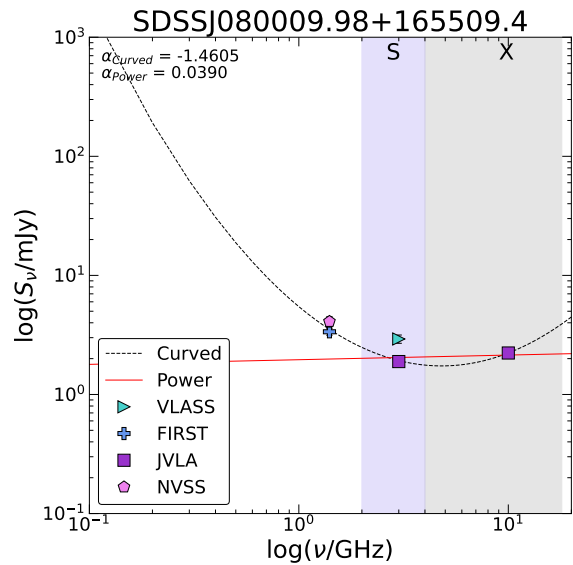
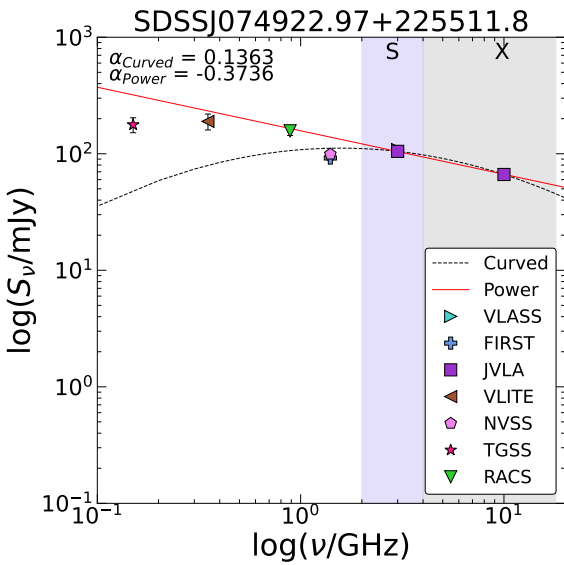
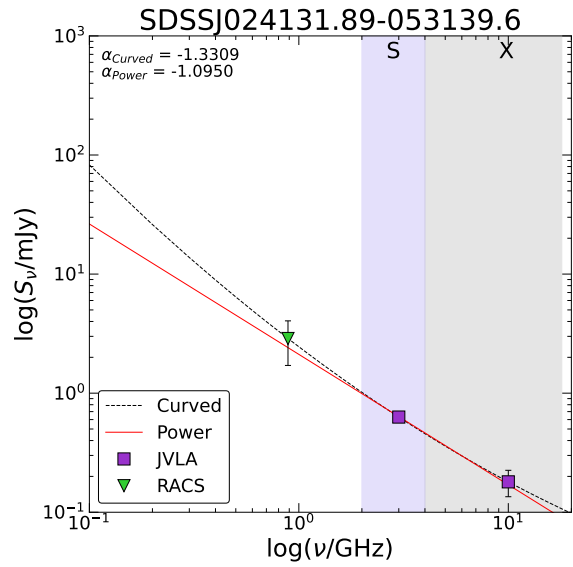
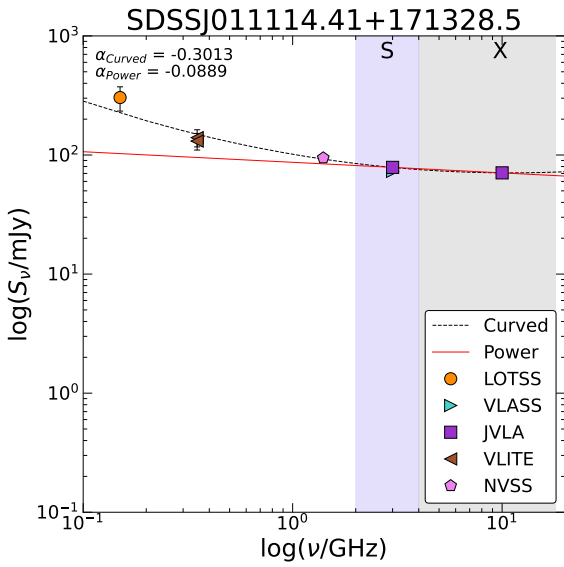
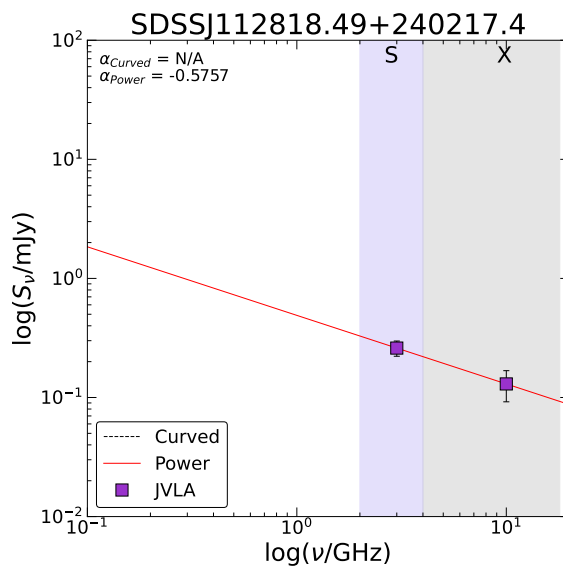
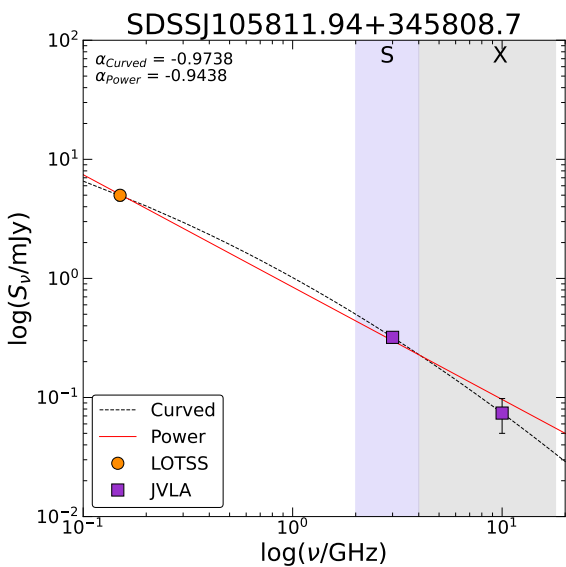
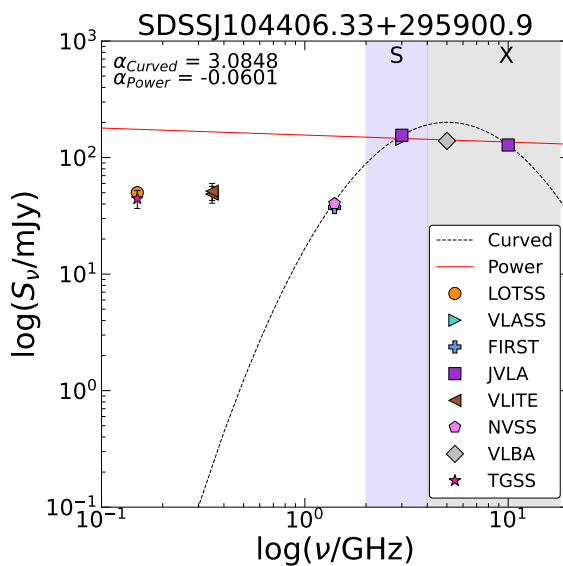
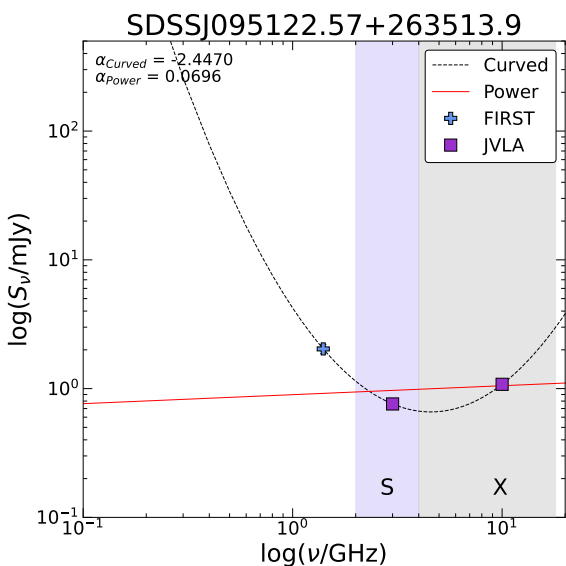
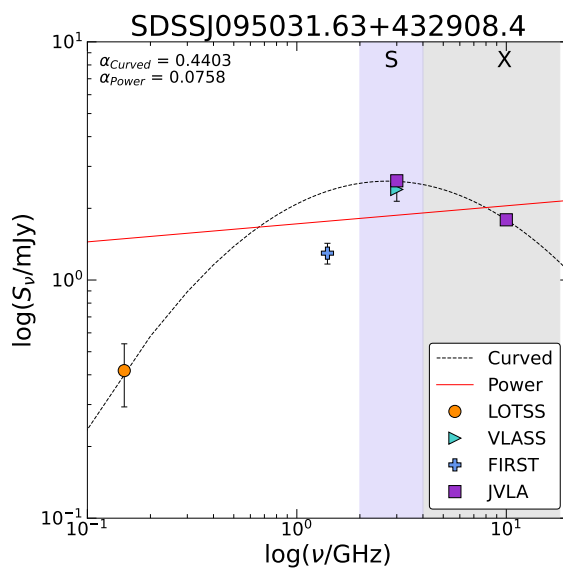
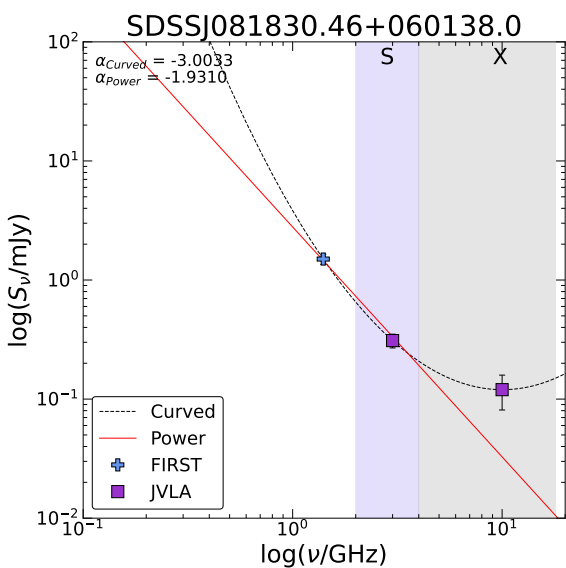
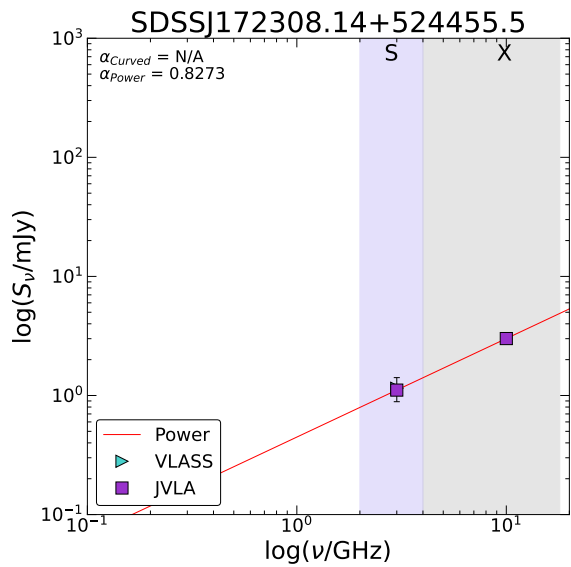
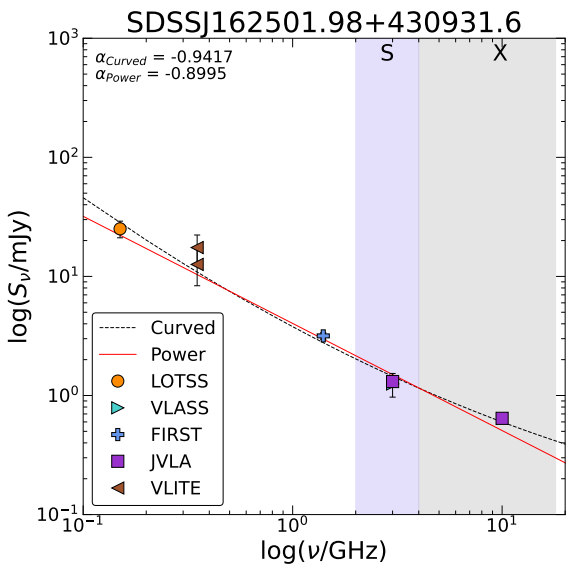
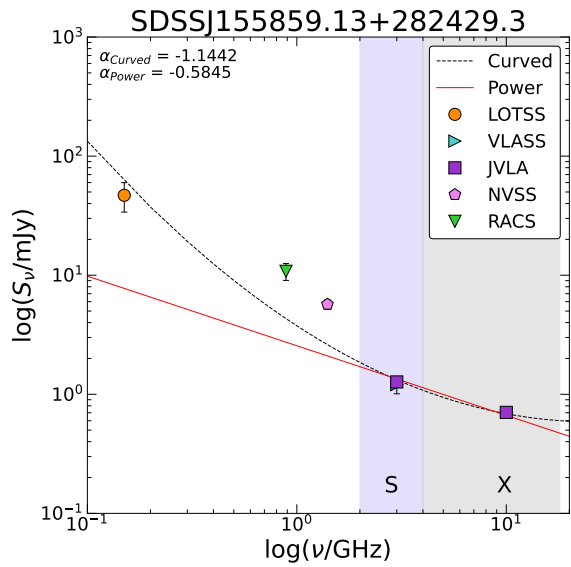
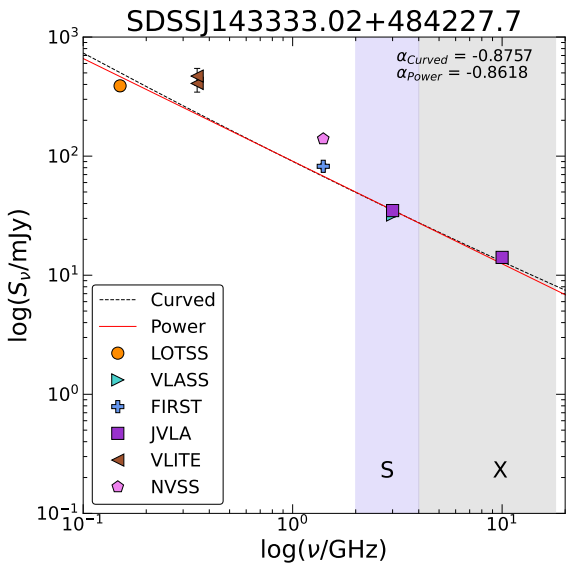
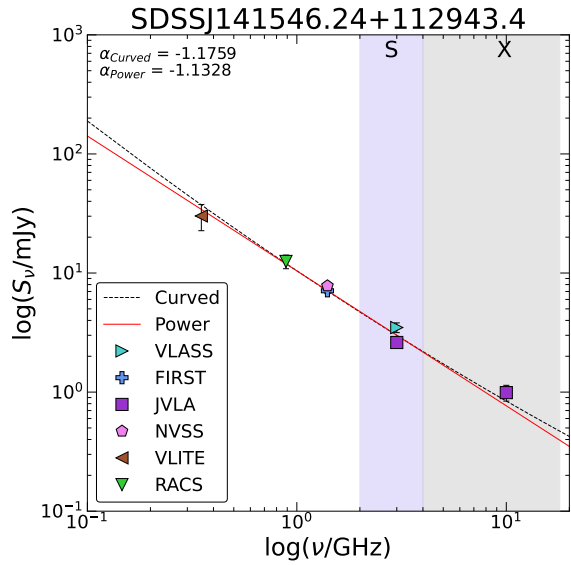
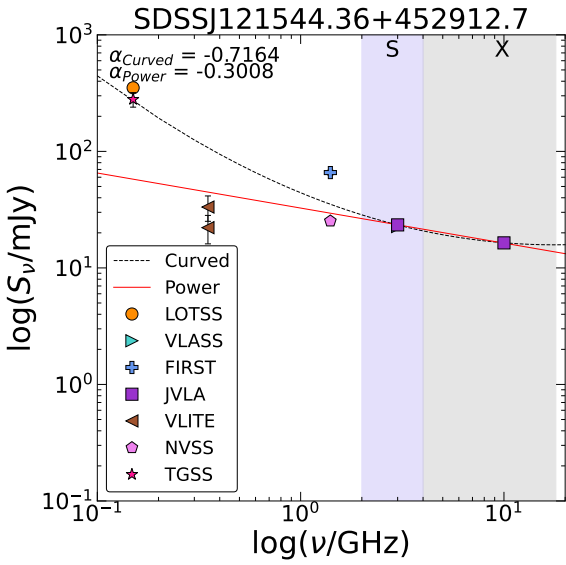


Figure 20. Optical tricolor ugz images drawn from the DeCaLS Legacy Viewer for the full sample. The SDSS designation for each object is listed in the top left corner of each panel, while the scale bar in the bottom right corner indicates 5''. Notice in several cases that the sources appear elongated rather than point-like, which may potentially point to underlying complex host morphologies and/or a multiplicity of sources, neither of which are not resolvable in these images.

12. APPENDIX D: RADIO SPECTRAL MODELING







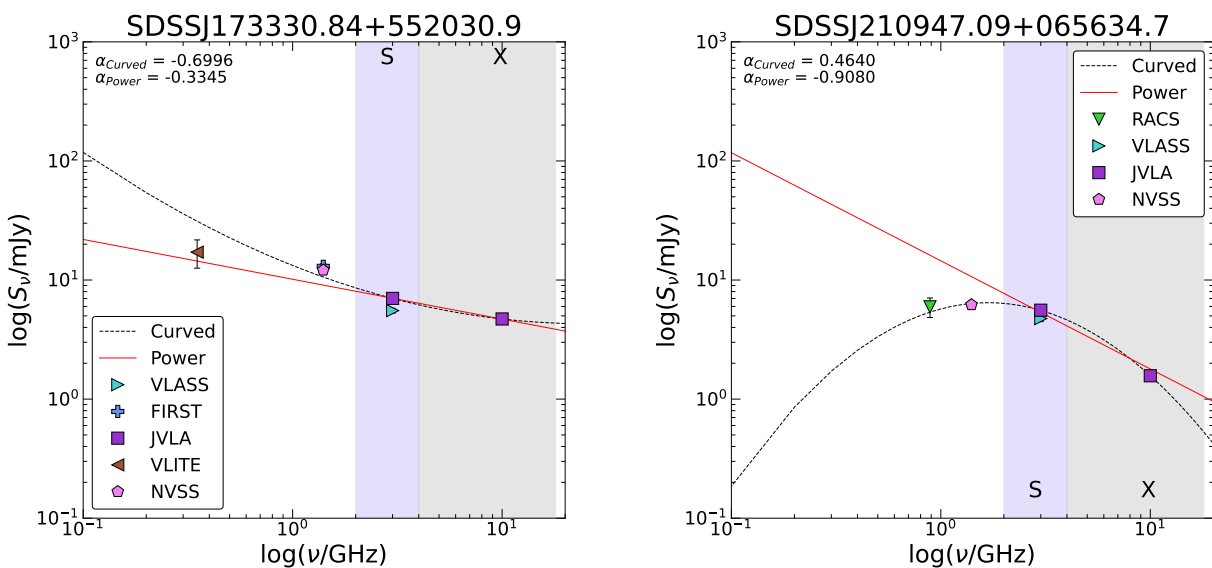


Figure 21. Broadband radio spectra showing the new, quasi-simultaneous VLA observations in purple squares, and the following archival measurements: VLASS (cyan, right-facing triangle), LOTSS (orange circle), FIRST (blue cross), VLITE (brown, left-facing triangle), NVSS (pink pentagon), VLBA (grey diamond), TGSS (hot pink star), and RACS (green, downward-facing triangle). For each source, the spectrum has been modeled with both a standard power law (red line) and a curved power law (dashed black line). The resultant spectral indices are listed.